The Astrophysical Journal, 749:33 (21pp), 2012 April 10 doi:10.1088/0004-637X/749/1/33

THE HUBBLE WIDE FIELD CAMERA 3 TEST OF SURFACES IN THE OUTER SOLAR SYSTEM: THE COMPOSITIONAL CLASSES OF THE KUIPER BELT

Wesley C. Fraser and Michael E. Brown
Division of Geological and Planetary Sciences, California Institute of Technology, 1200 E. California Blvd., Pasadena, CA 91125, USA; fraserw@gps.caltech.edu
Received 2011 August 18; accepted 2012 January 30; published 2012 March 20

ABSTRACT

We present the first results of the Hubble Wide Field Camera 3 Test of Surfaces in the Outer Solar System. The purpose of this survey was to measure the surface properties of a large number of Kuiper Belt objects and attempt to infer compositional and dynamical correlations. We find that the Centaurs and the low-perihelion scattered disk and resonant objects exhibit virtually identical bifurcated optical color distributions and make up two well-defined groups of objects. Both groups have highly correlated optical and NIR colors that are well described by a pair of two-component mixture models that have different red components but share a common neutral component. The small, $H_{606} \gtrsim 5.6$ high-perihelion excited objects are entirely consistent with being drawn from the two branches of the mixing model, suggesting that the color bifurcation of the Centaurs is apparent in all small excited objects. On the other hand, objects larger than $H_{606} \sim 5.6$ are not consistent with the mixing model, suggesting some evolutionary process avoided by the smaller objects. The existence of a bifurcation amongst all excited populations argues that the two separate classes of object existed in the primordial disk before the excited Kuiper Belt was populated. The cold classical objects exhibit a different type of surface that has colors that are consistent with being drawn from the red branch of the mixing model, but with much higher albedos.

Key words: Kuiper belt: general – planets and satellites: composition – techniques: photometric

Online-only material: color figures

1. INTRODUCTION

Kuiper Belt objects (KBOs), planetesimals near and beyond the orbit of Neptune, are debris left over from the planet formation process that occurred in the early solar system. Because of the relatively large heliocentric distances, KBOs likely present some of the most pristine material available for astronomical study, and as such, the Kuiper Belt is often regarded as a sort of archaeological window into the early history of the outer solar system.

Many KBOs are trapped in mean-motion resonances with Neptune, or are on highly inclined and eccentric orbits (Trujillo & Brown 2001). This has been taken as strong evidence that the majority of KBO orbits are not primordial, but rather these objects likely formed closer to the Sun and have since been scattered onto their current orbits. Resonance sweeping during the smooth migration of Neptune was originally put forth as a possible mechanism responsible for populating the mean-motion resonances (Malhotra 1993). This process, however, typically produces a Neptune with too low an eccentricity (see Morbidelli et al. 2008, for a review). An alternative, and the currently favored process, is scattering and chaotic capture by an eccentric Neptune (see, for example, Levison et al. 2008).

It seems that the Kuiper Belt's current members have experienced a diverse range of dynamical histories and were delivered from a broad range of heliocentric distances. It has been the hope that a compositional study of KBOs would reveal a wealth of information, not just about their chemical makeup, but also about their past dynamical pathways and relative formation locations within the primordial disk.

Spectroscopic studies of KBOs have revealed that these objects fall into three general classes. Members of the Haumea collisional family, of which the KBO Haumea (136108) is the largest, all exhibit spectra with the deepest water-ice absorption features seen in the Kuiper Belt consistent with surfaces of nearly pure water-ice (Brown et al. 2007). Non-Haumea family members make up the remaining two classes. The largest KBOs are found to be volatile rich, bearing ices such as methane and nitrogen (Cruikshank et al. 1976; Schaller & Brown 2007a). The spectra of smaller objects are found to be linear in the wavelength range $\lambda \sim 0.5$–0.9 μm (Hainaut & Delsanti 2002; Fornasier et al. 2009) with varying optical colors. This slope flattens toward more neutral colors at $\sim$0.9–1 μm. The small KBOs are all found to be absent of any absorptions due to the volatile ices exhibited by the larger objects and might only show some amount of water-ice absorption (Barkume et al. 2008; Guilbert et al. 2009). This is in agreement with the volatile retention model presented by Schaller & Brown (2007b), which demonstrates that only the largest objects have sufficient gravity to retain their volatiles against sublimation over the age of the solar system.

While the lack of volatile ices on the surfaces of the smallest objects is understood, the colors of these objects remain enigmatic. Optical surveys have revealed two peculiar correlations between optical color and orbital elements. The Centaurs, objects that reside on orbits between Saturn and Neptune, exhibit a bimodality in their optical colors and fall into two distinctive groups: the blue group has optical colors $1 \lesssim (B-R) \lesssim 1.4$, and the red group has $1.6 \lesssim (B-R) \lesssim 2$ with no known objects in between (Tegler & Romanishin 2003; Tegler et al. 2008).

The classical objects, which reside on orbits between the 2:3 and 1:2 exterior mean-motion resonances with Neptune ($40 \lesssim a \lesssim 48$) and have low to moderate eccentricities, exhibit nearly unanimously red colors at low inclinations. At higher inclinations, on the other hand, the classical objects exhibit a broad range of colors with much bluer objects than those found at low inclinations (Doressoundiram et al. 2002; Peixinho et al. 2004, 2008).

It might be expected that a two-component model of water-ice and some red organic material would explain the surfaces of the small KBOs. Luu & Jewitt (1996) and Jewitt & Luu (2001) presented a model in which the surfaces of KBOs were governed by two competing processes. Cosmic-ray bombardment over time would lead to a dark red irradiation mantel rich in complex organic material, while impact gardening would dredge up fresh blue, non-irradiated ice. If successful, this simple model would imply that the optical colors, amount of water-ice absorption, and geometric albedos of KBOs would be correlated. It has been shown that this is not the case (Barkume et al. 2008). In addition, it has been shown that both components in binary KBO systems exhibit virtually identical optical colors (Benecchi et al. 2009) incompatible with such a model. No model to date has convincingly accounted for the surface properties exhibited by the small KBOs.

We have performed a large spectrophotometric survey with the *Hubble Space Telescope* (*HST*; Cycle 17, HST-GO-Program 11644). The survey, designated the Hubble/Wide Field Camera 3 Test of Surfaces in the Outer Solar System (H/WTSOSS), was designed to take advantage of the deep optical and NIR imaging capabilities introduced with the Wide Field Camera 3 (WFC3) to obtain high-quality measurements of both the optical color and water-ice absorption on a large sample of KBOs too faint to be observed with similar quality in the NIR from even the largest ground-based offerings. We present the primary results of this project here.

In Section 2, we present our sample selection, observational techniques, and data reduction methods. In Section 3, we present the results of our photometry. We find that the targets in our survey fall generally into two classes based on their surfaces and orbits. In Section 4, we discuss what insights can be gained from our observations about the formation of the Kuiper Belt. Finally, we present our conclusions in Section 5.

2. OBSERVATIONS AND DATA REDUCTIONS

In this section, we present our target sample and observation techniques. Additionally, we present our data reductions and the resultant photometry acquired by the H/WTSOSS survey. The results of this survey along with previously published *HST* photometry of KBOs will be available online in database form at www.fraserkbos.com.

2.1. Target Selection and Classification

The primary goal of this survey was to gain optical and NIR spectroscopic information on KBOs too faint to be observed from the ground. Past NIR spectroscopic surveys have demonstrated an approximate ground-based magnitude limit of $V \sim 21$ (Barkume et al. 2008; Guilbert et al. 2009; Barucci et al. 2011). As such, with only a few exceptions, we restrict ourselves to objects with brightnesses below this level. Signal-to-noise estimates suggested that good-quality photometry could be acquired for objects as faint as $V \sim 24$, and we used this to bound our target list.

Effort was made to observe as diverse a range of KBOs as possible. Targets were selected from the Minor Planet Center (MPC; Bernstein 2008) based on their orbital quality to maximize the chances that the object would fall in the WFC3 field of view during Cycle 17. The result was a selection of 120 targets spanning the full range of orbital element space occupied by the Kuiper Belt. The observed targets are presented in Table 1. We present the orbital elements of our targets in Figure 1.

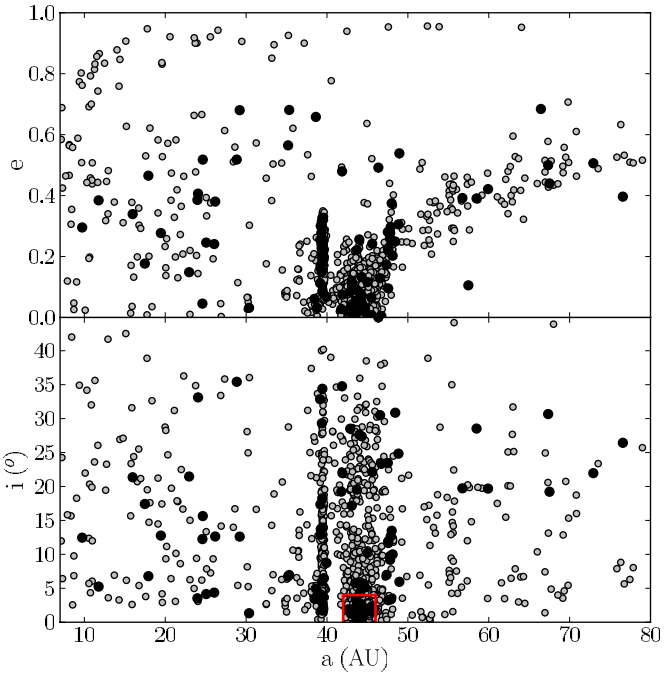

Figure 1. Eccentricity and inclination vs. semi-major axis of objects in the MPC (Bernstein 2008) (gray points) and the targets in this survey (black points). The red box shows the element space of the objects we designate as cold classical KBOs.

(A color version of this figure is available in the online journal.)

For completeness and historical reasons, we include orbital classifications for the observed objects. As shall be seen, however, the adopted orbital classification scheme has little bearing on the results of this work. We adopt an orbital classification scheme inspired by the system of Lykawka & Mukai (2007). We define Centaurs as those objects having semi-major axes $a < 30$ AU or perihelia $q < 25$ AU. We also define resonant objects as those objects in the 1:2, 2:3, 3:5, or 4:7 mean-motion resonances with Neptune.

It is well accepted that the non-resonant KBOs with semi-major axes bounded roughly by the 2:3 and 1:2 mean-motion resonances divide in inclination, i, into two populations (Brown 2001). Historically, these two populations, the hot and cold classical objects (CCOs), are defined as those objects with inclinations above and below $i = 5°$, respectively (Elliot et al. 2005). The CCOs, which all exhibit similar red surfaces, are on orbits with moderate eccentricities $e \lesssim 0.15$, while the hot classical objects (HCOs) exhibit a more diverse range of colors and eccentricities (see, for example, Peixinho et al. 2008). From a color standpoint, the inclination dividing these two populations is ambiguous. Dynamically, however, the inclination division is clear. Analysis of Figure 1 reveals a tight clump of objects with $i < 4°$ and $42 \lesssim a \lesssim 46$. For $i < 4°$, very few known non-resonant objects fall outside of this range in semi-major axis; none of these were observed in our survey. Thus, we adopt a definition for the CCOs, as those objects with $i < 4$ and $42 < a < 46$. We define HCOs as non-resonant objects with a bounded by the 1:2 and 2:3 mean-motion resonances, $i > 4°$, and $q > 37$ AU.

Those remaining objects not defined as Centaurs, resonant, CCOs, or HCOs are classified as scattered objects. It is worth noting that in some other works the scattered population is

Table 1
Survey Targets and Photometry

Designation[a]	a (AU)	i (°)	e	F606w	F814w	F139m	F153m	H_{606}
				Centaurs				
Nessus (1993 HA2)	24.64	15.63	0.51	23.30 ± 0.04	23.14 ± 0.04	24.08 ± 0.05	24.40 ± 0.05	9.800 ± 0.04
Hylonome (1995 DW2)	25.06	4.14	0.24	23.40 ± 0.04	23.71 ± 0.06	24.63 ± 0.08	24.94 ± 0.09	10.12 ± 0.06
Cyllarus (1998 TF35)	26.17	12.63	0.38	22.48 ± 0.02	22.38 ± 0.02	23.27 ± 0.02	23.53 ± 0.03	8.821 ± 0.02
29981 (1999 TD10)	98.15	5.95	0.87	21.98 ± 0.02	22.21 ± 0.02	23.36 ± 0.04	23.56 ± 0.03	9.032 ± 0.02
Elatus (1999 UG5)	11.76	5.24	0.38	22.43 ± 0.02	22.46 ± 0.02	23.64 ± 0.03	23.92 ± 0.04	10.92 ± 0.02
121725 (1999 XX143)	17.91	6.78	0.46	23.26 ± 0.04	23.34 ± 0.04	24.54 ± 0.07	24.85 ± 0.08	9.118 ± 0.04
60608 (2000 EE173)[b]	48.94	5.95	0.53	21.83 ± 0.1	22.09 ± 0.1	23.33 ± 0.02	23.57 ± 0.03	8.242 ± 0.1
87269 (2000 OO67)	657.7	20.05	0.96	...	...	...	...	...
87555 (2000 QB243)	35.19	6.76	0.56	23.00 ± 0.03	23.27 ± 0.04	24.26 ± 0.06	24.45 ± 0.06	9.067 ± 0.04
63252 (2001 BL41)	9.729	12.45	0.29	22.95 ± 0.03	23.22 ± 0.04	24.08 ± 0.05	24.33 ± 0.05	12.05 ± 0.04
88269 (2001 KF77)	26.05	4.36	0.24	23.82 ± 0.06	23.74 ± 0.06	24.57 ± 0.07	25.03 ± 0.09	10.69 ± 0.06
119315 (2001 SQ73)	17.47	17.42	0.17	22.03 ± 0.02	22.28 ± 0.02	23.31 ± 0.04	23.56 ± 0.04	9.645 ± 0.02
148975 (2001 XA255)	29.20	12.61	0.68	21.46 ± 0.02	21.71 ± 0.02	22.78 ± 0.02	23.01 ± 0.03	11.71 ± 0.02
Crantor (2002 GO9)	19.45	12.76	0.27	21.07 ± 0.02	21.11 ± 0.01	21.83 ± 0.01	22.11 ± 0.01	9.168 ± 0.01
2002 QX47	25.60	7.26	0.37	...	...	23.42 ± 0.03	23.69 ± 0.03	...
119976 (2002 VR130)	23.97	3.52	0.38	23.51 ± 0.04	23.80 ± 0.06	24.67 ± 0.08	25.02 ± 0.09	11.72 ± 0.06
127546 (2002 XU93)	66.44	77.96	0.68	21.72 ± 0.02	22.04 ± 0.01	23.08 ± 0.02	23.29 ± 0.02	8.497 ± 0.01
Ceto (2003 FX128)	99.85	22.32	0.82	21.85 ± 0.02	22.02 ± 0.01	22.96 ± 0.02	23.26 ± 0.02	6.888 ± 0.01
149560 (2003 QZ91)	41.86	34.76	0.47	23.13 ± 0.03	23.38 ± 0.04	24.28 ± 0.06	24.52 ± 0.06	8.800 ± 0.04
2004 QQ26	22.95	21.46	0.14	23.20 ± 0.04	23.53 ± 0.05	24.55 ± 0.07	24.82 ± 0.08	10.11 ± 0.05
160427 (2005 RL43)	24.59	12.24	0.04	22.03 ± 0.02	21.97 ± 0.01	22.85 ± 0.02	23.13 ± 0.02	8.288 ± 0.01
2005 RO43	28.84	35.42	0.51	21.62 ± 0.02	21.89 ± 0.01	22.80 ± 0.02	23.08 ± 0.02	7.527 ± 0.01
2005 VJ119	35.32	6.95	0.68	22.14 ± 0.02	22.32 ± 0.03	23.32 ± 0.04	23.62 ± 0.04	11.48 ± 0.03
2006 QP180	38.61	4.95	0.65	22.72 ± 0.04	22.57 ± 0.02	23.29 ± 0.02	23.83 ± 0.05	10.15 ± 0.02
2006 SQ372	1079.	19.45	0.97	21.94 ± 0.02	21.95 ± 0.01	22.98 ± 0.02	23.21 ± 0.02	8.132 ± 0.01
187661 (2007 JG43)	24.05	33.12	0.40	21.11 ± 0.01	21.39 ± 0.01	22.21 ± 0.02	22.35 ± 0.02	9.465 ± 0.01
2007 JK43	46.35	44.89	0.49	21.22 ± 0.01	21.41 ± 0.01	22.37 ± 0.02	22.62 ± 0.01	7.442 ± 0.01
2007 RH283	15.96	21.35	0.33	21.40 ± 0.01	21.68 ± 0.01	22.73 ± 0.02	23.00 ± 0.02	8.843 ± 0.01
				Scattered				
26308 (1998 SM165)	47.99	13.47	0.37	22.23 ± 0.03	22.13 ± 0.02	22.91 ± 0.02	23.18 ± 0.03	6.466 ± 0.02
69986 (1998 WW24)	39.49	13.93	0.22	23.88 ± 0.08	24.01 ± 0.08	24.86 ± 0.10	25.20 ± 0.11	8.695 ± 0.08
40314 (1999 KR16)	48.83	24.84	0.30	21.61 ± 0.02	21.48 ± 0.01	22.36 ± 0.01	22.68 ± 0.01	6.107 ± 0.01
1999 RJ215	59.91	19.68	0.42	23.06 ± 0.03	23.22 ± 0.04	24.13 ± 0.05	24.44 ± 0.06	7.706 ± 0.04
86177 (1999 RY215)	45.59	22.13	0.24	22.82 ± 0.03	23.17 ± 0.04	24.26 ± 0.06	24.43 ± 0.05	7.313 ± 0.04
91554 (1999 RZ215)	104.0	25.46	0.70	23.13 ± 0.03	23.35 ± 0.04	24.26 ± 0.06	24.58 ± 0.06	7.972 ± 0.04
2000 AF255	48.43	30.87	0.24	23.38 ± 0.04	23.17 ± 0.04	24.05 ± 0.05	24.40 ± 0.05	6.305 ± 0.04
2000 CQ105	56.74	19.72	0.39	23.26 ± 0.04	23.61 ± 0.05	24.66 ± 0.08	24.92 ± 0.09	6.548 ± 0.05
130391 (2000 JG81)	47.52	23.46	0.28	23.72 ± 0.05	23.90 ± 0.07	24.79 ± 0.09	25.09 ± 0.10	8.301 ± 0.07
2000 QL251	48.12	3.67	0.22	...	...	...	...	...
2000 YB2	38.76	3.82	0.03	23.05 ± 0.03	23.23 ± 0.06	24.14 ± 0.05	24.48 ± 0.06	7.198 ± 0.06
2000 YH2	39.22	12.90	0.30	22.63 ± 0.04	22.95 ± 0.03	24.21 ± 0.08	24.42 ± 0.05	8.273 ± 0.03
82158 (2001 FP185)	214.0	30.83	0.83	...	...	23.03 ± 0.02	23.33 ± 0.02	...
82155 (2001 FZ173)	84.97	12.73	0.61	...	...	22.86 ± 0.02	23.15 ± 0.02	...
2001 QR322	30.36	1.32	0.03	23.21 ± 0.04	23.51 ± 0.05	24.51 ± 0.07	24.79 ± 0.08	8.510 ± 0.05
2001 QX322	58.49	28.53	0.39	22.97 ± 0.03	23.16 ± 0.04	24.15 ± 0.05	24.46 ± 0.06	6.842 ± 0.04
2001 UP18	47.94	1.17	0.07	...	...	24.56 ± 0.07	24.82 ± 0.08	...
126155 (2001 YJ140)	39.37	5.98	0.29	22.17 ± 0.02	22.44 ± 0.02	23.38 ± 0.03	23.57 ± 0.03	7.764 ± 0.02
119979 (2002 WC19)	47.80	9.19	0.25	21.14 ± 0.01	21.19 ± 0.01	22.12 ± 0.01	22.38 ± 0.01	4.879 ± 0.01
2003 FE128	47.92	3.38	0.25	22.28 ± 0.02	22.34 ± 0.02	23.41 ± 0.03	23.67 ± 0.03	6.781 ± 0.02
2003 FF128	39.54	1.91	0.21	22.35 ± 0.02	22.34 ± 0.02	23.35 ± 0.03	23.69 ± 0.04	7.319 ± 0.02
2003 FJ127	44.02	22.93	0.22	...	...	...	...	...
2003 QA92	38.45	3.42	0.06	22.57 ± 0.02	22.62 ± 0.02	23.62 ± 0.03	23.84 ± 0.03	6.880 ± 0.02
2003 QX91	43.99	27.62	0.25	24.25 ± 0.08	24.49 ± 0.12	25.26 ± 0.14	25.66 ± 0.17	9.007 ± 0.12
2003 UY413	67.31	20.58	0.57	...	...	...	...	...
Sedna (2003 VB12)	510.2	11.92	0.85	...	...	21.99 ± 0.01	22.31 ± 0.01	...
2003 WU172	39.16	4.14	0.25	21.36 ± 0.01	21.46 ± 0.01	22.47 ± 0.01	22.74 ± 0.02	6.656 ± 0.01
120216 (2004 EW95)	39.36	29.30	0.31	21.18 ± 0.01	21.56 ± 0.01	22.68 ± 0.01	22.98 ± 0.02	6.796 ± 0.01
2004 PA108	54.57	1.14	0.46	...	...	...	...	...
2004 PA112	39.14	32.86	0.11	23.22 ± 0.04	23.55 ± 0.05	24.42 ± 0.06	24.63 ± 0.07	7.784 ± 0.05
2004 VN112	341.8	25.54	0.86	...	...	24.74 ± 0.09	24.95 ± 0.09	...
2004 XR190	57.47	46.66	0.10	22.14 ± 0.02	22.42 ± 0.02	23.46 ± 0.03	23.74 ± 0.03	4.545 ± 0.02
2005 EB299	51.76	0.71	0.50	...	...	...	...	...
2005 GE187	39.44	18.26	0.32	22.56 ± 0.02	22.55 ± 0.02	23.40 ± 0.03	23.62 ± 0.03	7.850 ± 0.02
2005 GF187	39.50	3.90	0.25	23.07 ± 0.03	23.43 ± 0.05	24.49 ± 0.07	24.77 ± 0.07	8.284 ± 0.05
2005 PU21	179.4	6.16	0.83	...	...	24.15 ± 0.05	24.39 ± 0.05	...
2005 RS43	48.11	9.99	0.20	21.72 ± 0.02	22.00 ± 0.01	23.11 ± 0.02	23.37 ± 0.02	5.464 ± 0.01

Table 1
(Continued)

Designation[a]	a (AU)	i (°)	e	F606w	F814w	F139m	F153m	H_{606}
145474 (2005 SA278)	92.90	16.25	0.64	22.73 ± 0.03	23.03 ± 0.03	24.21 ± 0.05	24.48 ± 0.06	6.724 ± 0.03
145480 (2005 TB190)	76.58	26.43	0.39	21.32 ± 0.01	21.46 ± 0.01	22.59 ± 0.01	22.90 ± 0.01	4.703 ± 0.01
2005 TV189	39.42	34.39	0.18	22.95 ± 0.03	23.21 ± 0.04	24.08 ± 0.05	24.31 ± 0.05	7.967 ± 0.04
2006 QH181	67.51	19.22	0.43	23.76 ± 0.05	23.80 ± 0.06	24.46 ± 0.07	24.63 ± 0.07	4.640 ± 0.06
225088 (2007 OR10)	67.34	30.67	0.49	21.67 ± 0.02	21.36 ± 0.01	22.06 ± 0.01	22.46 ± 0.01	2.335 ± 0.01
2007 TA418	72.92	21.96	0.50	23.26 ± 0.04	23.46 ± 0.05	24.41 ± 0.06	24.73 ± 0.07	7.622 ± 0.05
Resonant[c]								
118228 (1996 TQ66)	39.51	14.64	0.12	...	...	...	...	...
137295 (1999 RB216)	47.87	12.66	0.29	22.68 ± 0.03	22.82 ± 0.03	23.91 ± 0.04	24.15 ± 0.04	7.456 ± 0.03
60620 (2000 FD8)	43.68	19.54	0.22	22.86 ± 0.03	22.83 ± 0.03	23.54 ± 0.03	23.91 ± 0.03	7.047 ± 0.03
2000 FV53	39.18	17.35	0.16	23.25 ± 0.04	23.69 ± 0.06	24.69 ± 0.08	24.85 ± 0.08	8.020 ± 0.06
131318 (2001 FL194)	39.22	13.72	0.17	23.32 ± 0.04	23.60 ± 0.05	24.65 ± 0.08	24.80 ± 0.08	8.152 ± 0.05
2001 FQ185	47.57	3.24	0.22	23.25 ± 0.04	23.12 ± 0.03	24.11 ± 0.05	24.33 ± 0.05	7.613 ± 0.03
139775 (2001 QG298)	39.61	6.48	0.19	22.54 ± 0.02	22.56 ± 0.02	23.59 ± 0.05	23.88 ± 0.05	7.590 ± 0.02
2002 GY32	39.45	1.80	0.08	23.30 ± 0.04	23.38 ± 0.04	24.38 ± 0.06	24.60 ± 0.06	7.757 ± 0.04
2004 EH96	39.30	3.13	0.27	23.19 ± 0.03	23.11 ± 0.03	24.17 ± 0.07	24.44 ± 0.06	8.555 ± 0.03
2004 TV357	47.81	9.76	0.27	22.55 ± 0.02	23.00 ± 0.03	24.11 ± 0.05	24.39 ± 0.05	7.031 ± 0.03
2005 CA79	47.57	11.66	0.22	21.29 ± 0.01	21.45 ± 0.01	22.46 ± 0.01	22.72 ± 0.01	5.606 ± 0.01
2005 EZ296	39.35	1.77	0.14	22.89 ± 0.03	22.89 ± 0.03	23.91 ± 0.04	24.23 ± 0.05	7.456 ± 0.03
2005 GB187	39.43	14.69	0.23	22.25 ± 0.02	22.52 ± 0.03	...	...	7.415 ± 0.03
Hot classical								
1999 CL119	46.71	23.34	0.00	23.08 ± 0.03	23.18 ± 0.04	24.40 ± 0.06	24.66 ± 0.07	6.416 ± 0.04
2000 OH67	44.44	5.62	0.02	24.12 ± 0.07	24.17 ± 0.09	25.06 ± 0.16	25.39 ± 0.19	7.751 ± 0.09
150642 (2001 CZ31)	45.00	10.23	0.11	22.20 ± 0.02	22.58 ± 0.02	23.60 ± 0.03	23.84 ± 0.03	6.122 ± 0.02
2001 FO185	46.39	10.65	0.11	...	...	...	...	...
2001 HY65	43.06	17.16	0.11	22.64 ± 0.02	22.73 ± 0.02	23.73 ± 0.04	24.03 ± 0.04	6.689 ± 0.02
2001 KA77	47.56	11.91	0.09	22.61 ± 0.02	22.50 ± 0.02	23.39 ± 0.04	23.70 ± 0.04	5.779 ± 0.02
2001 PK47	39.93	8.73	0.06	23.48 ± 0.04	23.63 ± 0.05	24.65 ± 0.08	24.75 ± 0.07	7.748 ± 0.05
2001 QC298	46.56	30.50	0.12	22.68 ± 0.03	23.11 ± 0.05	24.14 ± 0.05	24.41 ± 0.05	6.639 ± 0.05
2001 QR297	44.69	5.13	0.03	23.47 ± 0.04	23.42 ± 0.04	24.41 ± 0.06	24.58 ± 0.09	7.068 ± 0.04
2002 PD155	43.49	5.75	0.01	23.97 ± 0.06	24.22 ± 0.13	24.93 ± 0.10	25.30 ± 0.12	7.687 ± 0.13
2003 LD9	47.36	6.97	0.17	23.35 ± 0.04	23.30 ± 0.04	24.38 ± 0.06	24.62 ± 0.07	7.198 ± 0.04
2003 QF113	44.10	4.45	0.03	23.61 ± 0.05	23.59 ± 0.05	24.73 ± 0.09	24.88 ± 0.08	7.348 ± 0.05
2003 SQ317	42.87	28.51	0.08	22.70 ± 0.03	23.22 ± 0.06	24.64 ± 0.08	26.01 ± 0.23	6.818 ± 0.06
2003 UZ117	44.29	27.39	0.13	21.39 ± 0.01	21.87 ± 0.01	23.39 ± 0.03	24.62 ± 0.06	5.462 ± 0.01
90568 (2004 GV9)	41.90	21.97	0.07	20.25 ± 0.01	20.391 ± 0.009	21.45 ± 0.01	21.70 ± 0.01	4.369 ± 0.00
145452 (2005 RN43)	41.77	19.24	0.02	20.16 ± 0.01	20.298 ± 0.009	21.40 ± 0.01	21.65 ± 0.01	4.044 ± 0.00
Cold classical								
1998 WY24	43.14	1.91	0.03	23.57 ± 0.05	23.64 ± 0.05	24.61 ± 0.08	24.88 ± 0.08	7.394 ± 0.05
2000 CE105	43.72	0.54	0.05	23.90 ± 0.06	23.81 ± 0.06	24.80 ± 0.09	24.98 ± 0.09	7.762 ± 0.06
123509 (2000 WK183)	44.37	1.96	0.04	23.11 ± 0.03	23.19 ± 0.04	24.22 ± 0.05	24.46 ± 0.06	6.814 ± 0.04
2000 WT169	44.87	1.74	0.01	22.80 ± 0.03	22.87 ± 0.03	23.83 ± 0.04	24.13 ± 0.04	6.303 ± 0.03
2000 WW12	44.74	2.49	0.12	...	...	...	...	...
88268 (2001 KK76)	42.60	1.88	0.02	23.33 ± 0.04	23.26 ± 0.04	24.14 ± 0.05	24.29 ± 0.05	7.093 ± 0.04
160147 (2001 KN76)	43.71	2.64	0.08	23.32 ± 0.04	23.38 ± 0.04	24.47 ± 0.07	24.70 ± 0.07	7.310 ± 0.04
2001 OQ108	45.52	2.32	0.00	23.79 ± 0.05	23.72 ± 0.06	24.73 ± 0.09	24.97 ± 0.09	7.231 ± 0.06
2001 QS322	44.28	0.24	0.04	23.65 ± 0.05	23.67 ± 0.06	24.71 ± 0.08	24.87 ± 0.08	7.413 ± 0.06
Teharonhiawako (2001 QT297)	44.29	2.57	0.02	22.83 ± 0.03	22.91 ± 0.04	23.97 ± 0.04	24.16 ± 0.04	6.302 ± 0.04
2001 QX297	44.42	0.90	0.03	23.42 ± 0.04	23.35 ± 0.04	24.37 ± 0.06	24.67 ± 0.07	7.060 ± 0.04
2001 RW143	43.21	2.96	0.03	23.90 ± 0.06	24.01 ± 0.08	...	...	7.711 ± 0.08
2001 RZ143	44.23	2.11	0.06	22.99 ± 0.03	23.06 ± 0.03	24.05 ± 0.05	24.33 ± 0.05	6.883 ± 0.03
2002 CU154	43.55	3.35	0.05	23.64 ± 0.05	23.65 ± 0.06	24.76 ± 0.09	25.18 ± 0.11	7.546 ± 0.06
2002 FW36	42.74	2.35	0.02	...	...	24.84 ± 0.09	25.15 ± 0.11	...
2002 PV170	42.93	1.27	0.01	22.80 ± 0.03	22.80 ± 0.03	23.83 ± 0.04	24.09 ± 0.04	6.530 ± 0.03
2003 GH55	44.12	1.10	0.07	22.63 ± 0.02	22.65 ± 0.02	23.53 ± 0.03	23.79 ± 0.03	6.529 ± 0.02
2003 HG57	43.55	2.10	0.03	22.70 ± 0.04	22.75 ± 0.03	23.94 ± 0.06	23.99 ± 0.05	6.368 ± 0.03
2003 QZ111	43.27	2.65	0.06	...	...	...	...	...
2006 HW122	45.48	1.53	0.06	23.99 ± 0.06	24.04 ± 0.08	24.97 ± 0.11	25.46 ± 0.14	7.558 ± 0.08

Notes. All magnitudes are presented in the STMAG system.

[a] MPC designations or names and asteroid numbers (where available). H_{606} is the absolute magnitude of the object determined from its observed magnitude in the F606w filter and its distance at time of observation.

[b] F606w and F814w photometry determined from observations presented by Benecchi et al. (2011; see Section 2.2).

[c] Resonant classifications generously provided by Brett Gladman (Gladman et al. 2008).

divided into groups: those objects on orbits that allow them to have interactions with Neptune, and those that are now well isolated from Neptune (see Gladman et al. 2008). Only two of our survey targets, which we classify as scattered, are not on interaction orbits. Therefore, we avoid this additional subclassification as an unnecessary complication for the purposes of this manuscript. Modifications to our classifications or the adoption of dynamically motivated and more complicated schemes such as that presented by Gladman et al. (2008) do not affect our conclusions.

2.2. Observations and Data Reductions

The primary scientific purpose of H/WTSOSS was to determine optical slopes and amount of water-ice absorption on faint KBOs. The excellent photometric stability of *HST* along with the imaging capabilities and filter selection of WFC3 made this new camera the ideal instrument for the job.

Each target was observed in exactly the same way. During the observations, the telescope was slewed at the apparent rate of motion of the target. Each target was visited only once and monitored for the entire visibility window of a single orbit. This ensured that no significant rotational variability would affect our photometry between different filters. Pairs of images were taken in the F606w, F814w, F139m, and F153m bandpasses with exposure times of 129 s and 453 s in each of the optical and NIR filters, respectively. Dithers of 3″ were included between each image of a pair to ensure that the photometry was not affected by cosmic rays or bad regions of a detector. The detectors were windowed to minimize overheads and to ensure the data could be transferred from the telescope during Earth occultation. This resulted in small square fields of view of 20.″5 and 131″ on a side for the optical and NIR images. As a result, eight objects fell outside the optical windows and were only seen in the NIR images. In six cases, the objects were not seen in the optical or NIR images entirely. In addition, six objects fell near enough to bright background sources to prevent reliable photometry in at least a few images. These images were excluded from our analysis (see Table 1).

Images were first processed through the standard WFC3 data processing pipeline, CalWF3 (Rajan et al. 2010). As of publication, all data presented here were processed using version 2.3 of this pipeline. Images were then visually inspected, and bad pixels and cosmic-ray strikes not identified during the initial processing were flagged.

Analysis of the *Tiny Tim* version 7.1 (Krist 1993) simulated point-spread functions (PSFs) revealed that the simulated PSFs did an adequate job of reproducing the outermost features of the observed PSFs (first airy ring, diffraction spikes, etc.) but failed to reproduce the image cores. As the majority of source flux is contained within the PSF core, photometry derived from matching *Tiny Tim* PSFs to the observations was deemed unreliable.

Photometry was derived using standard aperture photometry techniques. Aperture radii were chosen as a function of source brightness and wavelength to minimize measurement scatter. To minimize the effects of bad pixels and cosmic rays, *Tiny Tim* PSFs were used to interpolate over any bad pixels identified in the CalWF3 processing. Typically, only 1 pixel per aperture was flagged as bad. In addition, the simulated PSFs were used to derive infinite aperture corrections for each object. As the aperture radii were kept larger than the radius of the first airy ring, any errors introduced from the simulated PSF cores were negligible.

In a few cases, partially resolved binary sources were identified. In those cases, an aperture large enough to encompass both sources was used, and the combined photometry of both sources is reported. The adopted photometric system is the STMAG system. The STMAG system defines an equivalent flux density for a source with a spectrum that is flat as a function of wavelength that would produce the observed count rate. The magnitude in this system is just $\mathrm{STMAG} = -2.5 \log f_\lambda - Z$, where Z is the filter zero point and f_λ is the flux density expressed in erg cm^{-2} s^{-1} Å^{-1}. The resultant photometry is presented in Table 1, along with object colors in Table 2.

Object 2000 EE173 (60608) fell within the IR field of view but outside the UVIS field of view during observations. Optical data from Benecchi et al. (2011) in the F675w and F814w filters were available for this, from which a reliable estimate of the F606w and (F606w–F814w) color could be made. Conversion was done using an analog solar star and the *synphot* routine. We note that by estimating the F606w flux of 2000 EE173 in this way may introduce errors due to rotational variability. Duffard et al. (2009) have shown that the majority of non-Centaur KBOs have peak-to-peak light-curve amplitudes of $\lesssim$0.1 mag. As such, the photometric errors reported by Benecchi et al. (2011) were set to 0.1 mag to roughly account for any errors in estimating the F606w flux. This result is presented along with our other photometry in Table 2. No IR observations in the literature could be used to accurately determine F139m and F153m photometry of those objects that fell outside the IR field of view.

2.3. Photometric Uncertainties

In the case of photometry in either the flux- or background-limited regimes, the uncertainty in the observed magnitude, m, of a source can be well approximated by

$$\Delta m \sim \gamma 10^{\frac{m-Z}{2.5}}, \quad (1)$$

where Z is the photometric zero point of the passband in question. Theoretically, the proportionality constant γ is a function of the telescope and detector parameters such as gain, read noise, and data reduction parameters such as aperture size. In practice, this parameter is a factor of a few larger than the theoretical expectation (see, for instance, Newberry 1991; Fraser et al. 2008). In addition, theory underestimates the photometric scatter in repeated measurements of bright objects (see Figure 2). As a result, we consider an additional constant, C, and represent our photometric uncertainty by

$$\Delta m = C + \gamma 10^{\frac{m-Z}{2.5}}. \quad (2)$$

This equation is fit to the observed scatter from the dithered images of each source and each passband. The results of this procedure along with the best-fit parameters are presented in Figure 2. As can be seen, Equation (2) provides an adequate description of the measurement scatter in the photometry. It can also be seen that approximately 1% of measurements deviate significantly away from the curves given by Equation (2), primarily as a result of cosmic-ray strikes affecting one of the measurements of a pair. Thus, if the difference in pairs of observed magnitudes for a given filter was larger than 1.4 times the direct sum of errors of the pair of measurements, then it was assumed that the brighter of the two measurements was affected by a nearby cosmic-ray strike and was subsequently rejected.

The photometries presented here are average values from the pairs in each filter, or the single value when a measurement was

Table 2
Observed Colors

Designation	F606w–F814w	F814w–F139m	F139m–F153m
	Centaurs		
Nessus (1993 HA2)	0.156 ± 0.05	-0.94 ± 0.06	-0.31 ± 0.07
Hylonome (1995 DW2)	-0.31 ± 0.07	-0.91 ± 0.10	-0.31 ± 0.12
Cyllarus (1998 TF35)	0.095 ± 0.03	-0.88 ± 0.03	-0.25 ± 0.04
29981 (1999 TD10)	-0.23 ± 0.03	-1.14 ± 0.04	-0.20 ± 0.05
Elatus (1999 UG5)	-0.02 ± 0.03	-1.18 ± 0.04	-0.27 ± 0.05
121725 (1999 XX143)	-0.07 ± 0.06	-1.20 ± 0.08	-0.30 ± 0.11
60608 (2000 EE173)[a]	-0.26 ± 0.14	-1.23 ± 0.10	-0.23 ± 0.04
87269 (2000 OO67)	...	...	...
87555 (2000 QB243)	-0.26 ± 0.05	-0.99 ± 0.07	-0.18 ± 0.08
63252 (2001 BL41)	-0.27 ± 0.05	-0.85 ± 0.06	-0.25 ± 0.07
88269 (2001 KF77)	0.085 ± 0.08	-0.83 ± 0.10	-0.46 ± 0.12
119315 (2001 SQ73)	-0.25 ± 0.03	-1.02 ± 0.04	-0.25 ± 0.06
148975 (2001 XA255)	-0.24 ± 0.03	-1.07 ± 0.03	-0.22 ± 0.04
Crantor (2002 GO9)	-0.04 ± 0.03	-0.71 ± 0.02	-0.28 ± 0.01
2002 QX47	...	...	-0.26 ± 0.04
119976 (2002 VR130)	-0.28 ± 0.08	-0.87 ± 0.10	-0.34 ± 0.13
127546 (2002 XU93)	-0.32 ± 0.02	-1.03 ± 0.03	-0.20 ± 0.03
Ceto (2003 FX128)	-0.17 ± 0.02	-0.94 ± 0.02	-0.30 ± 0.03
149560 (2003 QZ91)	-0.24 ± 0.06	-0.90 ± 0.07	-0.23 ± 0.08
2004 QQ26	-0.33 ± 0.06	-1.01 ± 0.09	-0.27 ± 0.11
160427 (2005 RL43)	0.065 ± 0.02	-0.88 ± 0.02	-0.28 ± 0.03
2005 RO43	-0.27 ± 0.02	-0.90 ± 0.02	-0.27 ± 0.03
2005 VJ119	-0.18 ± 0.04	-0.99 ± 0.05	-0.30 ± 0.06
2006 QP180	0.146 ± 0.05	-0.71 ± 0.03	-0.53 ± 0.06
2006 SQ372	-0.00 ± 0.02	-1.03 ± 0.02	-0.22 ± 0.03
187661 (2007 JG43)	-0.27 ± 0.02	-0.82 ± 0.02	-0.13 ± 0.03
2007 JK43	-0.19 ± 0.02	-0.96 ± 0.02	-0.24 ± 0.02
2007 RH283	-0.28 ± 0.02	-1.04 ± 0.02	-0.27 ± 0.02
	Scattered		
26308 (1998 SM165)	0.104 ± 0.04	-0.78 ± 0.03	-0.27 ± 0.04
69986 (1998 WW24)	-0.13 ± 0.11	-0.84 ± 0.12	-0.34 ± 0.15
40314 (1999 KR16)	0.125 ± 0.02	-0.87 ± 0.02	-0.32 ± 0.02
1999 RJ215	-0.16 ± 0.05	-0.91 ± 0.06	-0.30 ± 0.08
86177 (1999 RY215)	-0.34 ± 0.05	-1.08 ± 0.07	-0.16 ± 0.08
91554 (1999 RZ215)	-0.21 ± 0.06	-0.90 ± 0.07	-0.32 ± 0.09
2000 AF255	0.211 ± 0.06	-0.88 ± 0.06	-0.34 ± 0.07
2000 CQ105	-0.34 ± 0.07	-1.04 ± 0.10	-0.26 ± 0.12
130391 (2000 JG81)	-0.18 ± 0.09	-0.88 ± 0.12	-0.29 ± 0.14
2000 QL251	...	...	...
2000 YB2	-0.18 ± 0.07	-0.90 ± 0.08	-0.33 ± 0.08
2000 YH2	-0.32 ± 0.05	-1.25 ± 0.08	-0.21 ± 0.10
82158 (2001 FP185)	...	...	-0.29 ± 0.03
82155 (2001 FZ173)	...	...	-0.29 ± 0.03
2001 QR322	-0.29 ± 0.06	-0.99 ± 0.09	-0.28 ± 0.11
2001 QX322	-0.18 ± 0.05	-0.99 ± 0.06	-0.30 ± 0.08
2001 UP18	...	...	-0.26 ± 0.11
126155 (2001 YJ140)	-0.26 ± 0.03	-0.93 ± 0.03	-0.19 ± 0.04
119979 (2002 WC19)	-0.04 ± 0.02	-0.93 ± 0.01	-0.25 ± 0.02
2003 FE128	-0.05 ± 0.03	-1.06 ± 0.03	-0.26 ± 0.04
2003 FF128	0.007 ± 0.03	-1.01 ± 0.03	-0.33 ± 0.05
2003 FJ127	...	...	...
2003 QA92	-0.05 ± 0.03	-0.99 ± 0.04	-0.22 ± 0.05
2003 QX91	-0.24 ± 0.14	-0.76 ± 0.18	-0.40 ± 0.22
2003 UY413	...	...	...
Sedna (2003 VB12)	...	...	-0.31 ± 0.02
2003 WU172	-0.09 ± 0.02	-1.00 ± 0.02	-0.27 ± 0.03
120216 (2004 EW95)	-0.38 ± 0.02	-1.11 ± 0.02	-0.29 ± 0.02
2004 PA108	...	...	...
2004 PA112	-0.32 ± 0.06	-0.87 ± 0.08	-0.20 ± 0.09
2004 VN112	...	...	-0.21 ± 0.12
2004 XR190	-0.27 ± 0.03	-1.04 ± 0.04	-0.28 ± 0.04
2005 EB299	...	...	...
2005 GE187	0.014 ± 0.03	-0.85 ± 0.04	-0.21 ± 0.04
2005 GF187	-0.36 ± 0.06	-1.05 ± 0.08	-0.27 ± 0.10

Table 2
(Continued)

Designation	F606w–F814w	F814w–F139m	F139m–F153m
2005 PU21	...	...	-0.23 ± 0.08
2005 RS43	-0.27 ± 0.02	-1.10 ± 0.03	-0.26 ± 0.03
145474 (2005 SA278)	-0.29 ± 0.04	-1.17 ± 0.06	-0.26 ± 0.08
145480 (2005 TB190)	-0.13 ± 0.02	-1.13 ± 0.02	-0.31 ± 0.02
2005 TV189	-0.25 ± 0.05	-0.87 ± 0.06	-0.22 ± 0.07
2006 QH181	-0.03 ± 0.08	-0.66 ± 0.09	-0.16 ± 0.10
225088 (2007 OR10)	0.301 ± 0.02	-0.69 ± 0.01	-0.40 ± 0.02
2007 TA418	-0.20 ± 0.06	-0.95 ± 0.08	-0.32 ± 0.10
Resonant			
118228 (1996 TQ66)	...	...	...
137295 (1999 RB216)	-0.14 ± 0.04	-1.09 ± 0.05	-0.24 ± 0.06
60620 (2000 FD8)	0.039 ± 0.04	-0.71 ± 0.04	-0.37 ± 0.05
2000 FV53	-0.43 ± 0.07	-0.99 ± 0.10	-0.15 ± 0.12
131318 (2001 FL194)	-0.28 ± 0.07	-1.04 ± 0.10	-0.15 ± 0.11
2001 FQ185	0.133 ± 0.05	-0.98 ± 0.06	-0.22 ± 0.07
139775 (2001 QG298)	-0.02 ± 0.03	-1.02 ± 0.05	-0.28 ± 0.07
2002 GY32	-0.08 ± 0.06	-0.99 ± 0.08	-0.22 ± 0.09
2004 EH96	0.078 ± 0.05	-1.05 ± 0.08	-0.27 ± 0.10
2004 TV357	-0.45 ± 0.04	-1.10 ± 0.06	-0.28 ± 0.07
2005 CA79	-0.15 ± 0.02	-1.01 ± 0.02	-0.26 ± 0.02
2005 EZ296	0.005 ± 0.04	-1.02 ± 0.05	-0.31 ± 0.06
2005 GB187	-0.27 ± 0.04	...	...
Hot classical			
1999 CL119	-0.10 ± 0.05	-1.21 ± 0.08	-0.25 ± 0.09
2000 OH67	-0.04 ± 0.11	-0.89 ± 0.19	-0.33 ± 0.25
150642 (2001 CZ31)	-0.37 ± 0.03	-1.01 ± 0.04	-0.24 ± 0.05
2001 FO185	...	...	...
2001 HY65	-0.08 ± 0.04	-0.99 ± 0.04	-0.30 ± 0.05
2001 KA77	0.113 ± 0.03	-0.89 ± 0.05	-0.31 ± 0.06
2001 PK47	-0.15 ± 0.07	-1.02 ± 0.10	-0.09 ± 0.11
2001 QC298	-0.43 ± 0.06	-1.03 ± 0.07	-0.26 ± 0.08
2001 QR297	0.048 ± 0.06	-0.98 ± 0.08	-0.16 ± 0.11
2002 PD155	-0.24 ± 0.15	-0.71 ± 0.17	-0.36 ± 0.16
2003 LD9	0.051 ± 0.06	-1.08 ± 0.08	-0.24 ± 0.09
2003 QF113	0.020 ± 0.07	-1.14 ± 0.10	-0.15 ± 0.12
2003 SQ317	-0.51 ± 0.06	-1.41 ± 0.10	-1.37 ± 0.24
2003 UZ117	-0.47 ± 0.02	-1.52 ± 0.03	-1.22 ± 0.07
90568 (2004 GV9)	-0.13 ± 0.01	-1.06 ± 0.01	-0.25 ± 0.01
145452 (2005 RN43)	-0.13 ± 0.01	-1.10 ± 0.01	-0.24 ± 0.01
Cold classical			
1998 WY24	-0.07 ± 0.07	-0.96 ± 0.10	-0.27 ± 0.11
2000 CE105	0.091 ± 0.09	-0.99 ± 0.11	-0.17 ± 0.13
123509 (2000 WK183)	-0.08 ± 0.05	-1.03 ± 0.07	-0.23 ± 0.08
2000 WT169	-0.07 ± 0.04	-0.95 ± 0.05	-0.29 ± 0.06
2000 WW12	...	...	...
88268 (2001 KK76)	0.072 ± 0.06	-0.88 ± 0.07	-0.15 ± 0.07
160147 (2001 KN76)	-0.06 ± 0.06	-1.08 ± 0.08	-0.23 ± 0.10
2001 OQ108	0.065 ± 0.08	-1.00 ± 0.11	-0.23 ± 0.13
2001 QS322	-0.01 ± 0.08	-1.04 ± 0.10	-0.15 ± 0.12
Teharonhiawako (2001 QT297)	-0.07 ± 0.05	-1.05 ± 0.06	-0.19 ± 0.06
2001 QX297	0.066 ± 0.06	-1.01 ± 0.08	-0.29 ± 0.09
2001 RW143	-0.10 ± 0.10	...	...
2001 RZ143	-0.07 ± 0.05	-0.99 ± 0.06	-0.27 ± 0.07
2002 CU154	-0.01 ± 0.08	-1.10 ± 0.11	-0.41 ± 0.14
2002 FW36	...	...	-0.31 ± 0.14
2002 PV170	0.004 ± 0.04	-1.02 ± 0.05	-0.26 ± 0.06
2003 GH55	-0.02 ± 0.04	-0.88 ± 0.04	-0.25 ± 0.05
2003 HG57	-0.04 ± 0.05	-1.19 ± 0.07	-0.04 ± 0.08
2003 QZ111	...	...	...
2006 HW122	-0.05 ± 0.10	-0.93 ± 0.13	-0.48 ± 0.18

Note. [a] (F606w–F814w) color determined from observations presented by Benecchi et al. (2011; see Section 2.2).

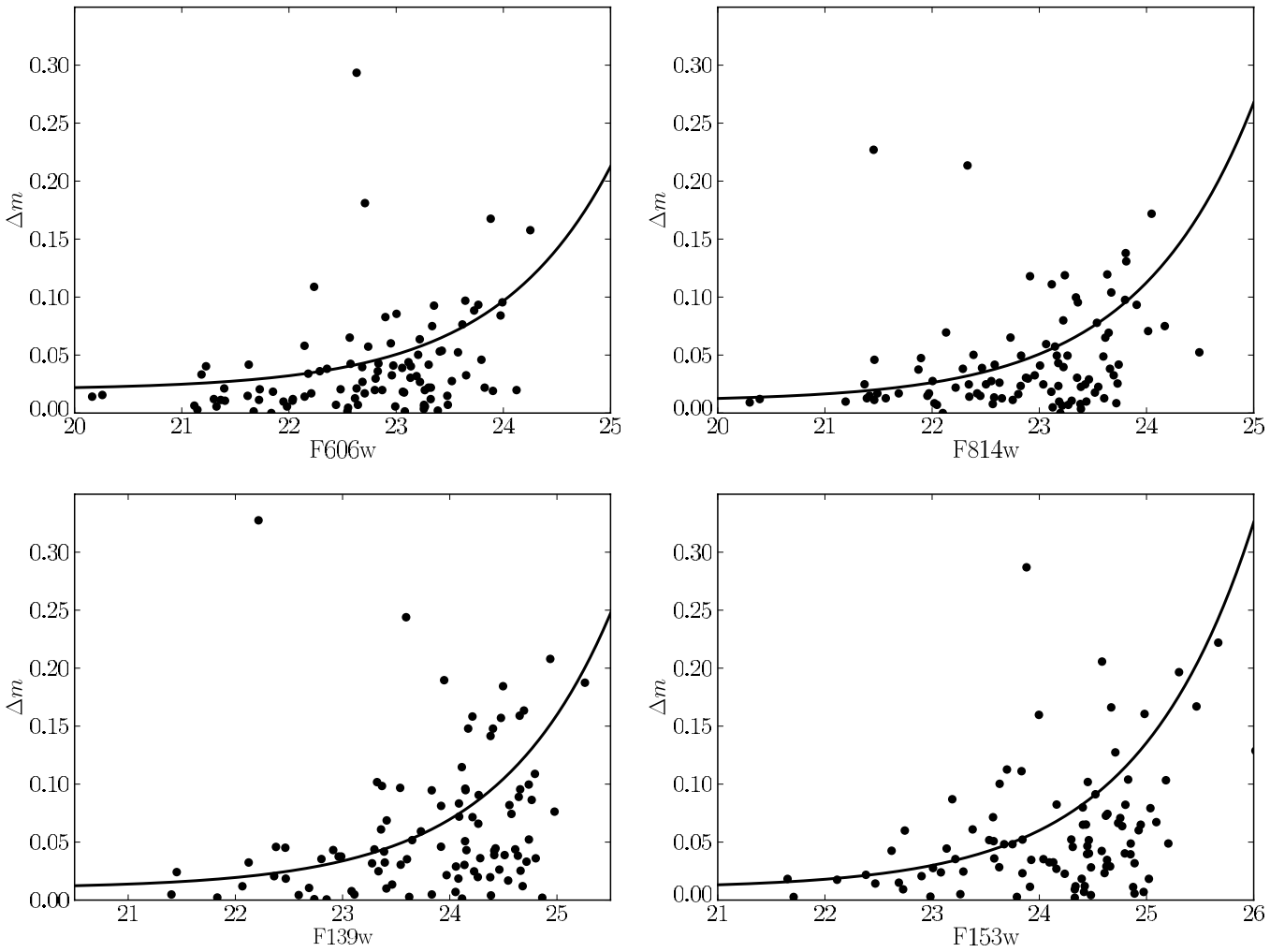

Figure 2. Scatter in the photometry from the image dither pairs vs. the average in the two measurements for all four filters. The curves represent the fit of Equation (2) to the presented data. Parameters (C, γ, Z) for these curves are (0.02, 0.6, 26.234), (0.01, 0.6, 25.918), (0.01, 0.6, 26.507), and (0.01, 0.6, 26.697) for the F606w, F814w, F139m, and F153m filters, respectively.

deemed bad, along with photometric uncertainties determined from the best-fit values of Equation (2) added in quadrature; the quoted photometric uncertainties represent 1σ errors.

3. RESULTS

In this section, we present the three color photometric results of the H/WTSOSS observations along with an interpretation of the observations in terms of a two-component mixing model. The main result is the identification of three types of KBO surface.

3.1. The Low Perihelia Objects

In Figures 3 and 4, we present the observed (F606w–F814w), (F814w–F193m), and (F139m–F154m) colors of the Centaurs. The well-known bifurcation of the optical colors of the Centaurs can be seen with the two color groups bifurcating about an optical color of (F606w–F814w) ~ -0.15. This bifurcation does not extend into the NIR in agreement with previous results (Tegler et al. 2008). It is interesting to note that the observed separation between the two groups is only $\sim$0.1 mag, much smaller than that found in previous surveys. Rather, we observe a few moderately colored Centaurs that have never before been detected in previous surveys of the Centaur population (Tegler et al. 2008; Benecchi et al. 2011).

Unlike the blue Centaurs, which exhibit a tight cluster, the red Centaurs span a broad swath of colors. This suggests that the red Centaurs exhibit a more diverse range of surfaces than do the blue Centaurs.

Analysis of ground-based colors suggests that the bifurcation exhibited by the Centaurs extends into the low-perihelion scattered disk and resonant objects. This can be seen in Figure 5, where we present the $(B-R)$ colors of objects with $q < 35$ AU taken from the MBOSS data set (Hainaut & Delsanti 2002). The H/WTSOSS photometry supports this finding. In Figure 6, we present the observed colors of all objects with perihelia $q < 35$ AU. This includes Centaurs and scattered, resonant, and HCOs. It can clearly be seen that most of the low-perihelia objects, which include resonant and scattered disk objects, occupy nearly the same range of colors as the Centaurs and exhibit the same bifurcation into two groups based on optical color. Only two H/WTSOSS targets, Elatus (1999 UG5) and 1999 XX143 (121725), are found to have optical colors between that of the blue and red Centaur groups. The ground-based colors of non-Centaur objects, on the other hand, have a higher fraction of objects with intermediate colors. These moderately colored objects, however, are predominately of objects with larger absolute magnitudes than in the Centaurs, suggesting that the larger objects do not exhibit the color bifurcation. Indeed,

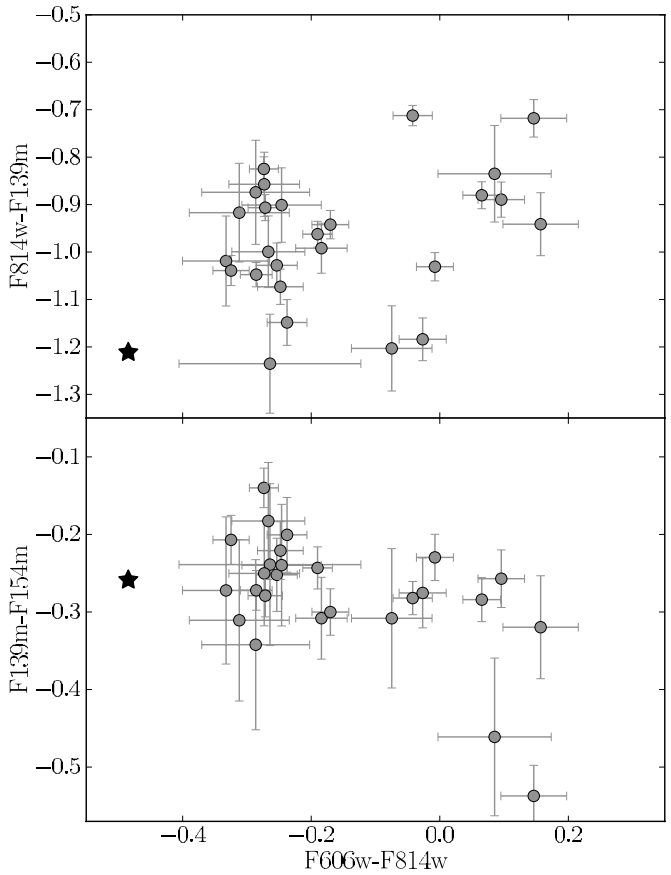

Figure 3. (F814w–F139m) and (F139m–F154m) vs. (F606w–F814w) colors of the Centaurs. Solar colors, $(\text{F606w–F814w})_\odot = -0.48$, $(\text{F814w–F139m})_\odot = -1.21$, and $(\text{F139m–F154m})_\odot = -0.26$ are shown by the star. Only those objects with good measurements in all four filters are shown.

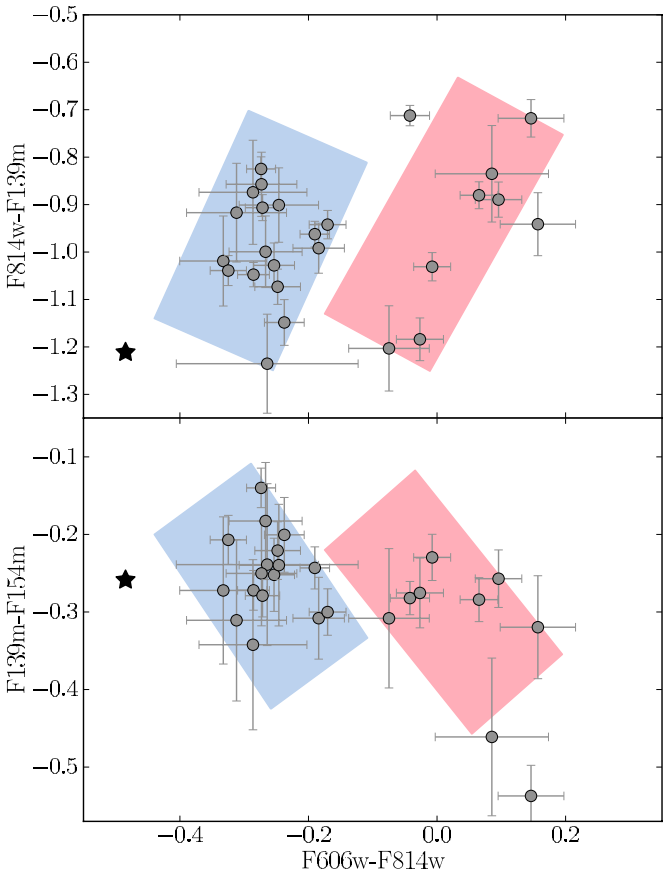

Figure 4. (F814w–F139m) and (F139m–F154m) vs. (F606w–F814w) colors of the Centaurs. Solar colors, $(\text{F606w–F814w})_\odot = -0.48$, $(\text{F814w–F139m})_\odot = -1.21$, and $(\text{F139m–F154m})_\odot = -0.26$ are shown by the star. Only those objects with good measurements in all four filters are shown. The extent of the red and blue shaded regions is selected to span the approximate extent of the red and blue classes of low-q object (see Section 3.1). These regions and the axis limits are the same for Figures 6, 10, 11, and 12 to ease comparison between them.

(A color version of this figure is available in the online journal.)

when only considering ground-based observations of objects with $H \gtrsim 6$ in the R band, in the same range as the Centaur H/WTSOSS targets, the bifurcation is more pronounced, suggesting that the largest objects occupy a different color range than the smaller bodies.

A clear outlier, 2007 OR10 is the reddest and largest object in the H/WTSOSS sample and is likely methane bearing (Brown et al. 2011a). As 2007 OR10 falls in a different class of object than the smaller methaneless objects, it is unsurprising that it appears as an outlier in Figure 6.

When considered together, the blue, (F606w–F814w) < -0.15 low-q objects appear as two distinct groups of objects, each of which exhibits highly correlated optical and NIR colors. The Spearman rank correlation test (Press 2002) suggests that for the blue group the (F606w–F814w) color correlates positively with the (F814w–F139m) color and negatively with the (F139m–F154m) color at the 99.8% and 99% significance levels, respectively (see Figure 6). Despite the wider range of colors, like their blue counterparts, the red low-q objects also exhibit correlated optical and NIR colors that have a 99% significance and correlate in a positive sense between (F606w–F814w) and (F814w–F139m) and in a negative sense between the (F606w–F814w) and (F139m–F154m) colors.

3.1.1. Mixing Models

A two-component mixing model can readily explain the range of observed colors of each color group of the low-q objects. We demonstrate the effectiveness of a compositional mixture with the use of a simple Hapke surface model. Here, we present a derivation showing only the necessary equations for our modeling. For a more thorough and complete derivation, see Hapke (2002).

We start with the wavelength-dependent particle single scattering albedo $w(\lambda)$. In the two-stream approximation, and under the assumption of irregular particles, the diffusive reflectance of the surface is given by

$$r_o = \frac{1-\gamma^*}{1+\gamma^*}, \tag{3}$$

where γ^* is the bulk albedo factor and is given by

$$\gamma^* = \sqrt{1-w(\lambda)}. \tag{4}$$

This equation is valid for an infinitely thick layer. Then, for a spherical object, covered by isotropically scattering particles, and ignoring the opposition effect, the geometric albedo can be approximated by

$$A(\lambda) \sim 0.49 r_o + 0.196 r_o^2. \tag{5}$$

Consider a mixture model of two components i and j. Each component will have a unique single scattering albedo, which

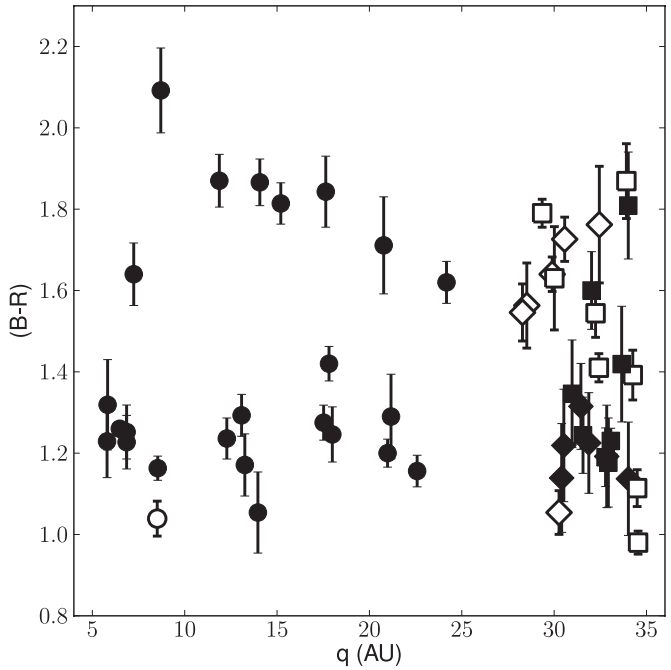

Figure 5. $(B-R)$ color vs. perihelion of the low-q Centaurs (circles), resonant objects (diamonds), and scattered disk objects (squares) in the MBOSS data set (Hainaut & Delsanti 2002). Only shown are those objects with measurement errors $\Delta(B-R) < 0.15$. Open and closed markers are those objects with absolute magnitudes larger or smaller than $H_R = 6.2$, respectively. The bifurcation in $(B-R)$ seen for the Centaurs seems to extend to higher perihelia for small KBOs.

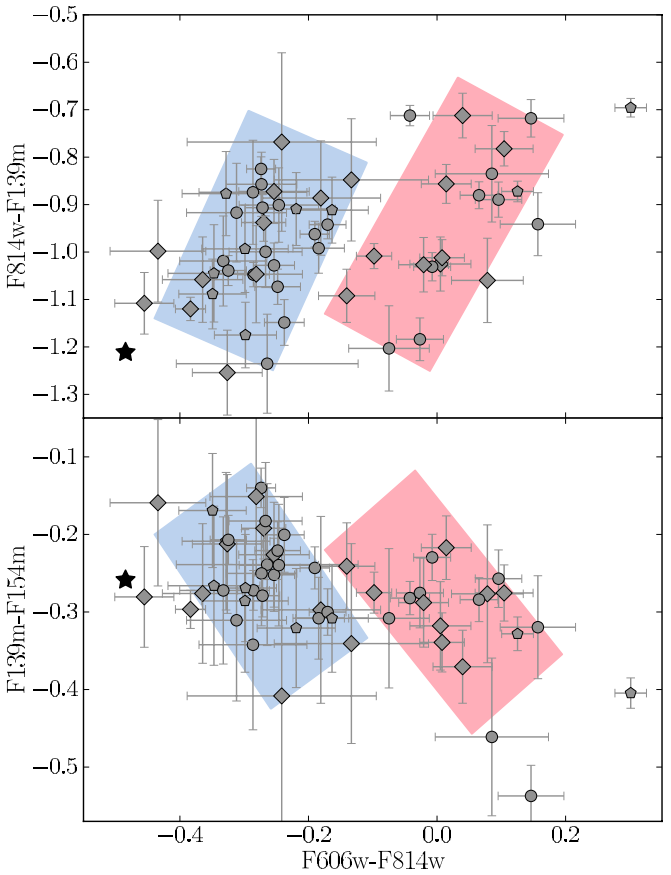

Figure 6. (F814w–F139m) and (F139m–F154m) vs. (F606w–F814w) colors of the Centaurs (circles), scattered disk objects (pentagons), and resonant objects (diamonds) with $q < 35$ AU. Solar colors are shown by the star. Only those objects with good measurements in all four filters are shown. The red and blue shaded regions show the approximately visual extent of the red and blue classes of low-q object. The shaded regions and axis limits are the same as those shown in Figure 4. The low-q objects consist of two separate classes of object.

(A color version of this figure is available in the online journal.)

we denote $w(\lambda)_i$ and $w(\lambda)_j$. These components can be mixed in two separate ways. The first, a geographic mixture, is one in which each component exists as discrete independent units on the surface. In this case, the effective albedo is just the fractional sum of albedos of each component given by Equation (5), or

$$A(\lambda)_{\rm geo} = f_{\rm geo} A(\lambda)_i + (1 - f_{\rm geo}) A(\lambda)_j \,, \quad (6)$$

where $f_{\rm geo}$ is the fraction of the surface occupied by component i.

Alternatively, the two components could exist as an intimate mixture, e.g., mineral material in an icy matrix. In this case, the effective single scattering albedo is the fractional sum of the single scattering albedos of each component and is given by

$$w(\lambda)_{\rm int} = f_{\rm int} w(\lambda)_i + (1 - f_{\rm int}) w(\lambda)_j \quad (7)$$

where $f_{\rm int}$ is the fraction of the surface occupied by component i. Thus, with a choice in w_i and w_j, Equations (6) and (7) and (5) produce not only a range of colors but also geometric albedos.

Analysis of Figure 6 suggests that the correlated colors of the blue and red groups of low-q objects might be explained by two separate mixing models that differ in their red components but share a common neutral component whose colors are nearly solar. We tested this possibility by fitting both the geographic and intimate mixture models to the observations. We assume two separate branches of a mixing model of the same type (geographic or intimate). In our model, each branch has a different red component, and we assume that both mixtures share the same nearly neutral component.

The geographic mixture requires nine parameters to describe all three observed colors simultaneously. These parameters are essentially the ratios of the single scattering albedos in each filter with respect to the F606w filter, three for each of the three components in our model. The intimate mixture requires two additional parameters describing the difference in single scattering albedos between each of the two red components and the neutral component. A change in these additional parameters results in a change in curvature of the resultant color curve.

The three component geographic and intimate mixture models were fit to the observations in a least-squares sense. We chose (F606w–F814w) $= -0.15$ to separate the objects belonging to the blue and red groups during our fits. It was also necessary to ensure that the resultant range of model colors was restricted to the range of observed colors of our targets. This action was taken to prevent runaway during the least-squares minimization. It should be emphasized that it cannot be determined whether the true colors are beyond this range by the observed colors alone.

The results of the model fitting to the 55 low-q objects in the H/WTSOSS sample are shown in Figures 7 and 8. As can be seen, the colors of the neutral and red components for both models are very similar. Both the intimate and geographic mixture models do an adequate job of describing the observations.

2007 JG43, 2004 EW95, and 2004 TV357, all blue low-q objects, along with red low-q objects Elatus (1999 UG5), Crantor (2002 GO9) and 2007 OR10, were all identified as outliers responsible for the vast majority of the fit residuals. Crantor has optical color very near but just redward of the

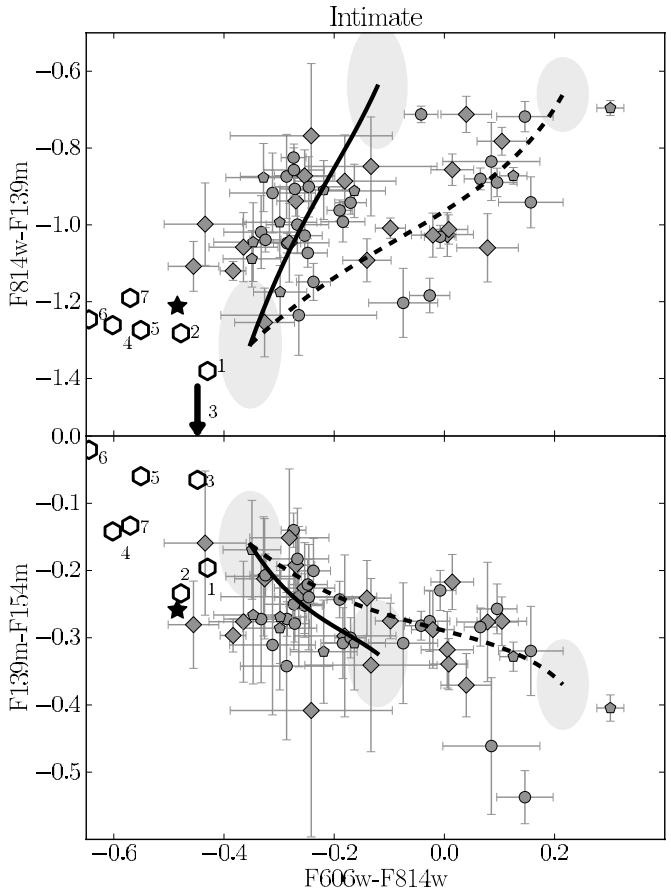

Figure 7. Same as in Figure 6 but with the colors predicted by the red and blue branches of the intimate mixture model shown as dashed and solid lines, respectively. The 3σ uncertainty range in the colors of both red- and the neutral-end components is shown as shaded regions. The colors of a selected range of silicates consistent with the inferred color of the neutral component are shown as open hexagons. 1, 2: chlorites CU91-238A, and GDS159; 3, 4: serpentines HS318.4B and HS8.3B; 5, 6: olivines GDS70.d and NMNH137044.b; 7: magnetite HS195.3B. The intimate mixture models fully describe the observed KBO colors.

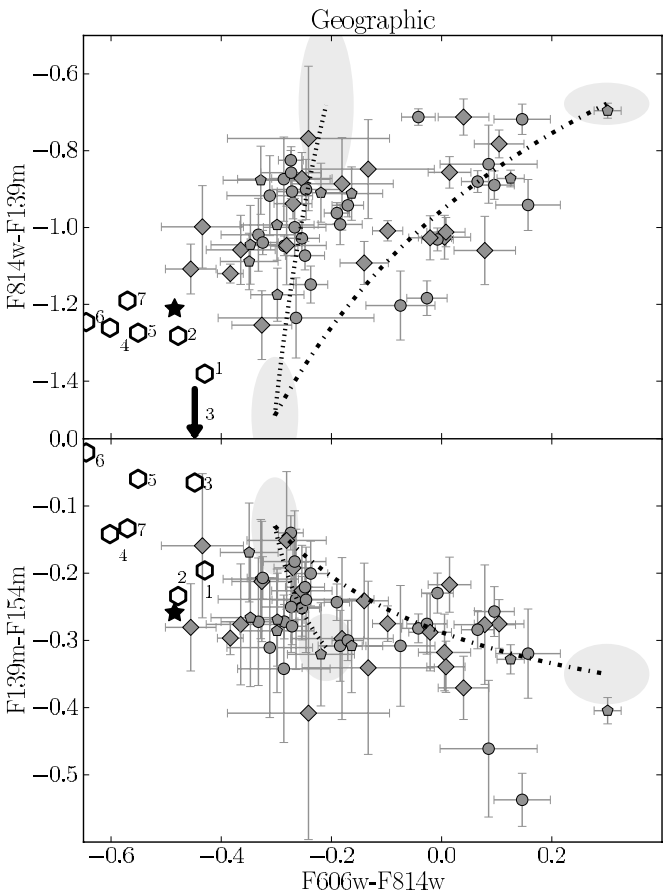

Figure 8. Same as in Figure 7 but with the colors predicted by the red and blue branches of the geographic mixture model shown as dash-dotted and dotted lines, respectively. The 3σ uncertainty range in the colors of both red- and the neutral-end components is shown as shaded regions. The colors of a selected range of silicates consistent with the inferred color of the neutral component are shown as open hexagons. 1, 2: chlorites CU91-238A, and GDS159; 3, 4: serpentines HS318.4B and HS8.3B; 5, 6: olivines GDS70.d and NMNH137044.b; 7: magnetite HS195.3B. Like the intimate mixture models, the geographic models well describe the observed KBO colors, but with higher residuals and one additional outlier.

(F606w–F814w) $= -0.15$ color chosen to separate the blue and red Centaurs. Given its NIR colors, however, Crantor is roughly equally consistent with either the red or blue branches of the mixing model. As discussed above, 2007 OR10 possesses a surface unique to the large volatile bearing KBOs, and it is therefore no surprise that it stands out from the majority. It is not unreasonable to expect other outliers as our simple mixing models do not consider other processes such as collisions that can alter surface colors. When the outliers are not considered in the fit, the resultant chi-squared values were reduced by nearly half compared to when the outliers were considered.

A similar finding as for Crantor exists for a few of the blue low-q objects. That is, objects placed in the blue group by our selected division are better described by the blue end of the red mixing curve. It is not clear, however, if this is a result of the limitations of our chi-squared fits. This possibility should be further studied with more observations, however, as the result would imply that the red Centaur population is not uniquely red, but rather occupies a range of optical colors that sparsely samples the blue end of the red mixing curve.

After excluding the six outliers, the model best fits had reduced chi-squared values of $\chi^2_{\nu,\,\mathrm{geo}} = 2.87$ and $\chi^2_{\nu,\,\mathrm{int}} = 3.13$ with 38 and 40 degrees of freedom for each model, respectively. The geographic model resulted in a reduction of the variance in the data of only 13%, while a reduction of 40% was found for the intimate mixture model. In addition, though the best-fit intimate mixture could account for the colors of 2006 QP160, the best-fit geographic model could not and rejected it as an additional outlier. Despite the two extra parameters, the intimate mixture model provides a better description of the data over the geographic model. These results suggest that intimate mixtures are a better model of the surfaces of the objects we observed compared to the geographic mixtures.

Typically, inference of KBO compositional makeup has been made through extensive spectral modeling of not only deep spectral lines diagnostic of particular materials but also the general spectroscopic shape not attributable to any one material (see Barucci et al. 2008, for a review). Materials required to successfully model featureless spectra of KBOs typically include organic materials such as tholins or other irradiated hydrocarbons, mineral components such as olivine, water-ice, and neutral darkening agents such as carbon (Cruikshank et al. 1998; Alvarez-Candal et al. 2008; Merlin et al. 2010; Barucci et al. 2011). The range of colors required by the components of our mixing model is compatible with many of these materials.

The red components require a material that is blue from ~1.3 to 1.5 μm. It is tempting to attribute this color to water-ice

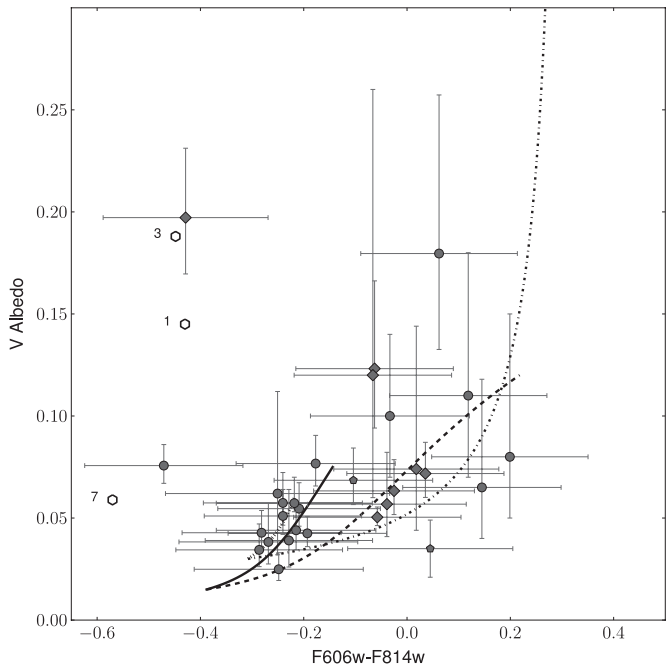

Figure 9. Geometric visible albedo vs. (F606w–F814w) color calculated from available ground-based optical colors from the MBOSS data set (Hainaut & Delsanti 2002) for small KBOs with $q < 35$ AU. Symbols are as in Figures 6, 10, and 12. The colors and albedos predicted by red and blue intimate and red and blue geographic mixture models that describe the low-q objects are shown as solid, dashed, and dash-dotted lines. The conversion from ground-based to *HST* filters was done using the solar analog colors produced by the *synphot iraf* routine, which results in a ∼0.15 mag uncertainty. The albedos of the silicates from Figure 7 are shown as hexagons. Those not visible have albedos higher than the range shown.

absorption. The red colors of each material for wavelengths $\lesssim$1.3 are compatible with the irradiated organic ices and tholins often attributed to the spectral shapes of other KBOs (Cruikshank et al. 1991; Brunetto et al. 2006). While no unique identification can be made from these observations, it seems plausible that the red components are different combinations of organic and water ices.

The range of colors of the neutral component requires a material that is virtually neutral across all four filters used in our observations. Due to the large absorption at ∼1.55 μm, water-ice is not a candidate. Rather, a plausible candidate for the neutral component appears to be silicates. The colors of various minerals taken from the USGS Spectral Library (Clark et al. 2007) are shown in Figures 7 and 8, along with their albedos in Figure 9. Minerals consistent in color with the inferred neutral component include olivines similar to those inferred from previous spectral modeling of KBOs (Merlin et al. 2010). Other compatible minerals include serpentines and aqueously altered phyllosilicates, the latter of which provide the best match to our fitted colors. The albedos of all of these silicate materials, however, are all too high to be consistent with the low $\rho \sim 5\%$ albedos of the blue Centaurs. Rather, some additional neutral darkening agent such as amorphous carbon is needed, as has been found in previous spectral modeling efforts (see, for instance, Cruikshank et al. 1998).

The candidate silicate materials we and others have presented are similar to the iron-rich minerals and hydrated silicates that have been suggested to exist on the largest, outermost Saturnian irregular satellite, Phoebe (Clark et al. 2005). Phoebe and the other irregular satellites are captured objects that likely originated from the same primordial population as the observed KBOs (Nesvorný et al. 2007). Thus, while no claim from our observations can be made as to what the neutral component may be, the apparent compositional similarity between Phoebe and the observed KBOs suggests that indeed these objects share a genetic link, and that the minerals we present are good candidates for the neutral material. If confirmed, this result would suggest that despite the large formation distances of KBOs and irregular satellites, aqueous alteration and therefore liquid water were prevalent in the outer solar system.

The best fits of the intimate mixture to the colors of the blue objects have a preference to models in which the red component shares a similar single scattering albedo to the blue component. The red objects, however, are better matched if the red component albedo of the red branch is significantly larger than that of the neutral component. Despite the poor availability of albedo measurements, many of which are thermal model dependent, our findings are in agreement with the observed trend in KBO albedo with color. We present measured albedos of KBOs (see Stansberry et al. 2008) versus their F606w–F814w color calculated from their observed colors taken from the MBOSS data set in Figure 9. This suggests that the reddest objects have higher albedos than the bluest objects. The observed colors and albedos are well reproduced by the intimate mixture model if the red components of the blue and red branches have albedos a factor of ∼2 and ∼4 times larger than that of the neutral component (assumed to be 3% in Figure 9). The geographic mixture model can also reproduce the albedo color trend but predicts that the reddest objects will have albedos $\gtrsim$25%, a factor of ∼3 higher than that predicted for the intimate model. Further observations are required to determine if such high albedos exist for reddest KBOs.

The chi-squared fits of the mixture models we present here have a few potential weaknesses. As stated above, the colors of the two components were restricted to prevent runaway during the minimization. As such, the true colors of the neutral and red components might be beyond the range of colors inferred from the fits. In addition, the model we present is rather simple and does not account for many processes that may affect the surfaces of KBOs. As such, the fits we present are best used as a guide to understanding the primary surface properties of objects in the Kuiper Belt rather than an exact description. Despite the model's simplicity, it is clear that two separate branches of a mixing model that shares a common—and neutral—component can account for the major trends in the observed colors of the low-perihelion KBOs. In addition, a model in which the components are mixed intimately appears to be favored over one in which the mixture is geographic.

3.2. The High-perihelion Objects

The observed colors of the hot classical, scattered, and resonant objects with $q > 35$ AU are shown in Figure 10. Other than the two identified Haumea family members, 2003 UZ117 and 2003 SQ317 (Schaller & Brown 2008; Snodgrass et al. 2010), much of the distant excited population is consistent in color with the intimate mixture model fit to the low-q population. The distant population, however, has a higher fraction of objects with moderate optical color, $-0.2 \lesssim$ (F606w–F814w) $\lesssim 0.0$, and suggests that the colors of the distant objects are not consistent with the intimate mixture model. No obvious hints of a bimodal population are apparent for the high-q objects.

We tested whether or not the non-Haumea family, high-q objects could be drawn from the mixture model of the low-q

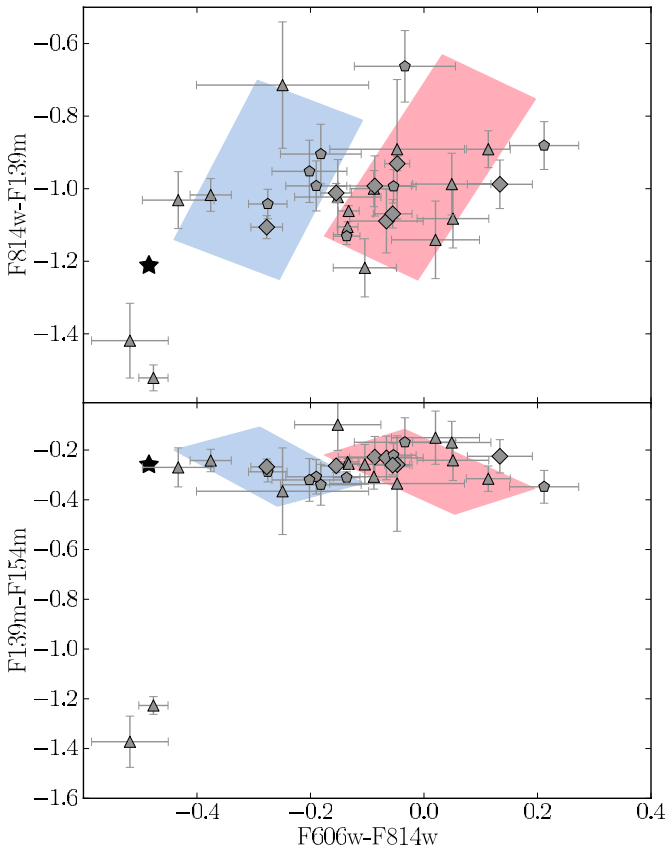

Figure 10. (F814w–F139m) and (F139m–F154m) vs. (F606w–F814w) colors of the Centaurs (black circles), scattered disk objects (pentagons), hot classical objects (diamonds), and resonant objects (diamonds) with $q > 35$ AU. Haumea family members 2003 UZ117 and 2003 SQ317 stand out as having very strong water-ice absorption. Solar colors are shown by the star. Only those objects with good measurements in all four filters are shown. The red and blue shaded regions approximately show the extent of the red and blue classes and are the same as those shown in Figure 4.

(A color version of this figure is available in the online journal.)

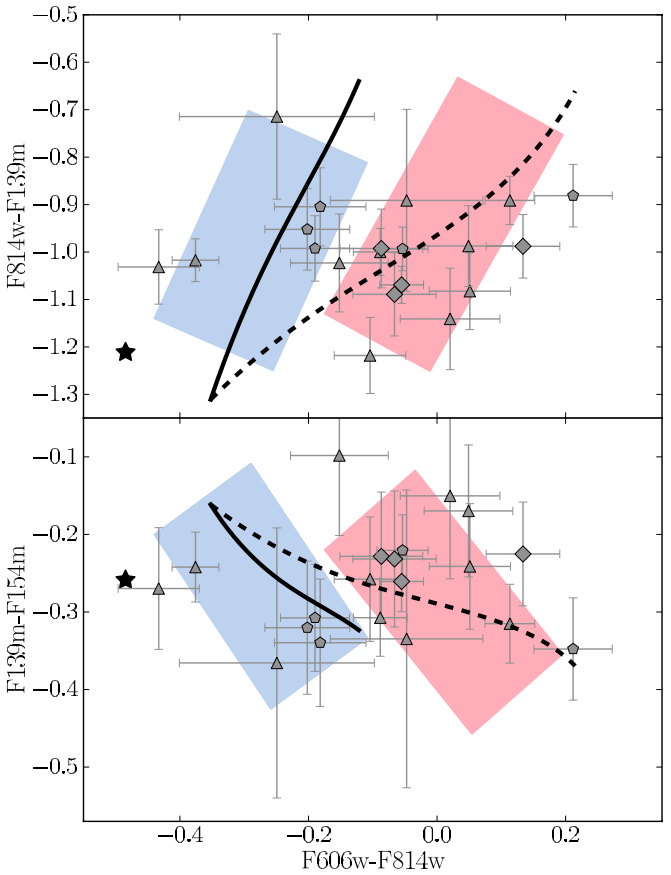

Figure 11. Same as in Figure 10 but only for those non-Haumea family member objects with $H_{606} > 5.6$. The blue and red intimate mixture models that describe the colors of the low-q objects are shown as solid and dashed lines, respectively. The red and blue shaded regions approximately show the extent of the red and blue classes of low-q objects. The shaded regions and axis limits are the same as those shown in Figure 4. The small, excited objects are consistent with being drawn entirely from the red and blue classes of low-q objects.

(A color version of this figure is available in the online journal.)

objects with a Monte Carlo technique. This involved drawing from the dual intimate mixture model, a sample of objects equal in number to the high-q population with the same ratio of red to blue objects. Gaussian scatter was added to the random colors with standard deviations equal to the observed uncertainties. Then, by adopting the observed uncertainty distribution, the intimate mixing model that was used to describe the low-q objects was refit to the random sample. This process was repeated 100 times, and the distribution of chi-squared values was recorded. In 90% of cases, the simulated chi-squared values were lower than the observed value, demonstrating that the model that describes the low-q objects does not match the observed high-q population.

As discussed above for 2007 OR10, the largest objects have a different color distribution than smaller objects. Using the observed absolute magnitude as a proxy for size, the observed high-q population contains objects with absolute magnitudes $4 \lesssim H_{606} \lesssim 8$, while the low-$q$ population, ignoring 2007 OR10, only has objects with $H_{606} > 6$. Indeed, the largest objects in our sample are the most discrepant. After rejecting the eight intermediate-sized objects with high-q objects with $H_{606} < 5.6$, the Monte Carlo test suggests that the probability of drawing a random chi-squared equal to or greater than the observed value for the remaining 20 objects is 35%; the colors of the small, high-q objects are consistent with being drawn from the intimate mixture model that describes the colors of the low-q objects. It should be noted that object 2001 CZ31 appears as an outlier. Indeed, when this object is rejected, the probability of drawing a random chi-squared equal to or greater than the observed value becomes 50%. However, rejection of this object as an outlier is not formally required by the model.

The colors of the small, excited, high-q population are shown in Figure 11. No bifurcation of the optical colors is apparent in this figure. It should be noted that this sample has uncertainties that are $\gtrsim$50% larger than the low-q sample. Thus, we should not expect to see the bimodality exhibited by the low-q objects. The observations we present here are not of sufficient quality to show the existence of such a bimodality. The colors of the small, excited, high-q objects, however, are consistent with the bimodal low-q population.

Our results suggest that only the largest objects in our high-q sample are inconsistent with the low-q population. The larger uncertainties could mask small changes in color between the two samples. If it is true that the small high-q objects possess the same color distribution as the low-q objects, this would suggest that little to no color evolution occurs when high-q objects are scattered into the Centaur region. Even if color evolution does occur, as typical color uncertainties are only of order 5%, the changes must be small.

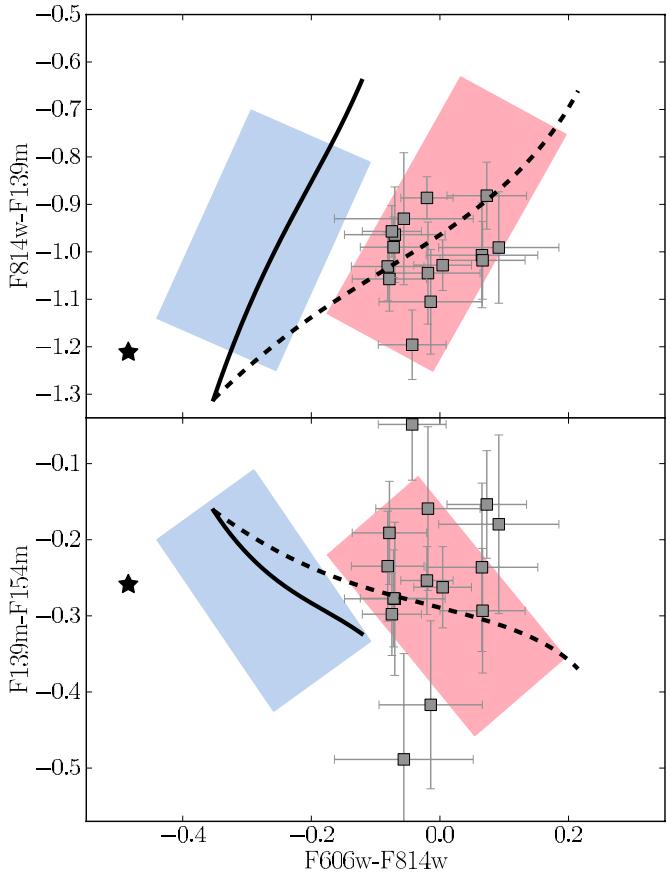

Figure 12. (F814w–F139m) and (F139m–F154m) vs. (F606w–F814w) colors of the cold classical objects, shown as red squares. Solar colors are shown by the star. Only those objects with good measurements in all four filters are shown. The red and blue intimate mixture models that describe the colors of the low-q objects are shown as dashed and solid lines, respectively. The red and blue shaded regions approximately show the extent of the red and blue classes of low-q objects. The shaded regions and axis limits are the same as those shown in Figure 4. The cold classical objects do not appear to be consistent with either class of excited object.

(A color version of this figure is available in the online journal.)

The largest objects in our sample have colors inconsistent with the two intimate mixtures that describe the low-q population. As these objects must have formed of the same material as the smaller objects, it must be that some processes that do not readily occur on smaller objects have altered the surfaces of the larger bodies. Our observations suggest that the size transition occurs at $H_{606} \sim 5.6$. Assuming a 6% albedo, this corresponds to objects with diameters $D \sim 400$ km. This also coincides with a transition in albedos; objects smaller than this size have lower albedos than larger objects. The larger, intermediate-sized objects are still too small to retain their primordial volatile budget as the largest known KBOs have. But for these intermediate-sized objects, effects such as the onset of differentiation could modify their surfaces. Whatever the cause might be, the apparent difference in colors between objects with absolute magnitudes smaller and larger than $H_{606} \sim 5.6$ clearly warrants confirmation.

The observed colors of the CCOs are presented in Figure 12. The well-known unique colors of this population are clear, lacking not only the reddest objects but also the entire blue group of objects observed in other KBO populations. Interestingly, with the exception of object 2003 HG57, the CCOs appear consistent in color with the red branch of the intimate mixture model that describes the low-q population, albeit with a narrower range of colors. Indeed, our Monte Carlo tests suggest that the colors of the CCOs are entirely consistent with the red branch of the mixture model; the probability of a randomly drawn chi-squared value greater than that observed is only 20% when 2003 HG57 is excluded.

Our observations alone would suggest that the CCOs and the red branch of the Centaurs and small excited KBOs share different mixtures of the same primordial materials. This simple picture is challenged by available albedo observations of these objects. Despite the sparser sampling and larger error bars, Brucker et al. (2009) have shown that the albedos of the CCOs $\gtrsim$0.15, inconsistent with that predicted from the red branch of the mixing model. The excited high-q objects, however, are fully consistent with the model and exhibit the same general trends in albedo as the low-q objects; the red objects appear to have higher and exhibit a wider range of albedos than do the blue objects, which all appear to have low albedos of ∼5%. Thus, while it appears that the small, excited populations of the Kuiper Belt are all drawn from either the red or blue branches of the mixing model, the CCOs are not. Higher quality albedo measurements are required to determine whether or not the CCOs possess a surface unique to this population alone.

3.3. Bifurcation Tests

In Section 3.1, we identified an apparent bifurcation in the colors of the low-q objects that is consistent with that observed in the ground-based optical colors of the Centaurs (Tegler et al. 2008). While the colors of all small, excited objects appear to exhibit this bifurcation, the significance of this feature and the physical model we put forth to explain it remain untested. We turn to the use of "blind" statistical tests, that is, tests that require no a priori information or user input to test if the data exhibit two separate populations, or are consistent with being drawn from a single population. The first test we turn to is the non-parametric bifurcation test commonly adopted in the literature pertaining to the colors of KBOs, Hartigan's DIP test (Hartigan & Hartigan 1985). The DIP test, however, is only one-dimensional. Thus, when utilizing the DIP test, we must only consider the optical color alone, where the data appear most bifurcated. For the multivariate data we present here, the one-dimensional DIP test is inappropriate.

We also consider multivariate clustering techniques. The first clustering technique we consider is hierarchical clustering using Ward's criterion (Everitt et al. 2011). Ward's criterion uses a sum of squares of cluster member distances from average cluster position as a clustering metric and typically results in same-sized, circular clusters. In addition, we consider the normal mixture model distribution clustering technique, which assumes underlying multivariate Gaussian distributions for each of the identified clusters. In a Bayesian formalism, this technique fits a chosen number of Gaussian components or clusters to the observed distribution, resulting in a best-fit likelihood, L. As such, the corrected Bayes information criterion (BIC), which can be approximated by $-2 \log L + p \log((n-2)/24)$, can be evaluated for different cluster numbers to provide subjective information as to the true number of clusters within the data. Here, p is the number of parameters in the fit (12 per Gaussian component in three dimensions), and n is the number of data points. That is, the number of clusters can be increased one at a time such that the resultant increase in the BIC is maximized. This provides the most likely number of clusters. Mixture model maximum likelihood fits to the data were performed with the *PyMix* package (Georgi et al. 2010). A review of these and

other common clustering techniques is available in Everitt et al. (2011).

We also consider the minimum spanning tree (MST) based technique, maximum standard deviation reduction (MSDR), presented by Grygorash et al. (2006). This technique is excellent at identifying clusters in small-sample, multivariate data sets and avoids the chaining effect to which other hierarchical and MST-based techniques are prone (Everitt et al. 2011)

Much like virtually all other clustering methods, however, the three clustering techniques mentioned above, hierarchical, mixture model, and MSDR, provide virtually no information as to the correct number of clusters in the observed data. When this information is available, it is subjective at best—no test of the significance of identified clusters is provided. To overcome this weakness, we introduce the *F optimal plane* or FOP-test. The FOP-test, which is also based on the MST of the data, uses a separate clustering statistic than MSDR to determine which edge to prune, resulting in two sub-clusters of the data. In addition, the resultant statistic F of the pruned edge provides a means of determining the significance that the two sub-clusters are consistent with the null hypothesis, that the data are consistent with a single population only. Thus, the FOP-test has a major advantage over other multivariate clustering techniques in that it provides quantitative information as to the number of extant clusters in the observed data.

A detailed discussion of the FOP-test and some examples of its performance versus the MSDR clustering technique are presented in the Appendix. The reader is warned that the FOP-test is an ad hoc combination of two alternative clustering metrics that remains to be mathematically proven. As is shown in the Appendix, however, the FOP-test performs just as well and often even outperforms the mathematically tested MSDR-based clustering technique in both correctly identifying the true number of clusters and correctly assigning cluster membership in various simulated data sets.

In Figures 13 and 14, we present the results of the blind statistical tests applied to the observed colors of the small, excited population, or those non-CCO, non-family member objects with $H > 5.6$. For this test, we further reject the data with error in (F6062–F814w) of 0.1 mag or larger to avoid biasing our results with poor-quality data.

In the (F606w–F814w) color alone, the small, excited sample appears bimodal; the DIP test confirms this with 98.6% chance of bimodality. The application of the hierarchical clustering technique with two clusters results in two clusters that exactly reflect the red and blue compositional classes identified in Sections 3.1 and 3.2. That is, those blue class members are all uniquely identified to one cluster, and those red class members are uniquely identified to the other cluster with no incorrect identifications.

Application of the normal mixture models paints a similar picture. The value of the BIC as the number of clusters is increased from 1 to 5 is a, b, c, d, and e with a maximal increase when the number of clusters is 3. The first two identified clusters are just the red and blue compositional classes. Most of the red objects fall into the first cluster, and most of the blue objects fall into the blue cluster, with only eight objects (six red and two blue) falling into the third cluster, which occupies nearly the full extent of the blue and red clusters combined. Thus, the normal mixture model clustering paints the same picture as we discuss above; the small, excited KBOs appear to exhibit compositional classes with a few outlier objects.

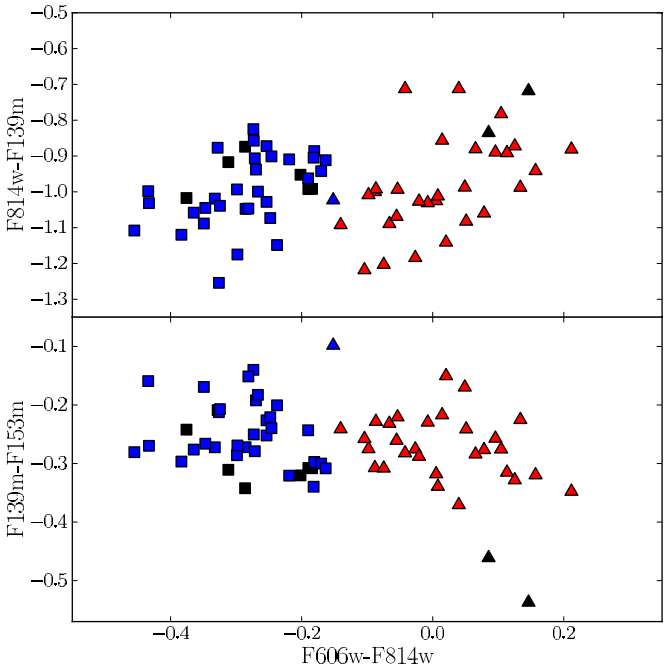

Figure 13. Results of the hierarchical clustering and normal mixture model clustering applied to the (F814w–F139m) and (F139m–F154m) vs. (F606w–F814w) colors of non-CCO, non-family member objects with $H > 5.6$ and error in (F814w–F139m) less than 0.1 mag. Error bars are omitted for clarity. Squares and triangles are objects classified as belonging to the two separate clusters identified by the hierarchical clustering. Blue, red, and black points are objects classified as belonging to the three separate clusters identified by the normal mixture model clustering. Both techniques agree with our assertion that most of the small, excited KBOs exhibit bifurcation into two separate classes at a color of (F606w–F814w) ~ -0.15.

(A color version of this figure is available in the online journal.)

The results of the FOP-test are in agreement with the hierarchical and normal mixture model results. The FOP-test identifies two clusters within the data—exactly the two classes we identified in Sections 3.1 and 3.2. The edge pruned by this method is the only edge of the MST that spans (F606w–F814w) $= -0.15$, the color that divides the two compositional classes. The results of the FOP-test agree; calibrating the result of the FOP-test by bootstrapping and by sampling from the uniform distribution demonstrates that the probability that the observed data are consistent with a single population is only 5% or 7%, respectively (see the Appendix for a discussion of these calibration methods).

The MSDR technique further strengthens this result. The first two sub-clusters found by this technique are those visually identified in Sections 3.1 and 3.2 and are identical to those found by the FOP-test. The stopping criterion of the MSDR technique is met when four clusters are produced. The FOP-test, however, demonstrates that further divisions beyond the first are insignificant, and only two populations are required.

Upon application of these blind tests to the Centaur and low-q populations, we find the same results, albeit with lower significance. Hartigan's DIP test suggests that the probability of bimodality is 85% and 67% for the Centaurs and low-q samples, respectively. The MSDR clustering and FOP-test both identify identical sub-populations, the same two classes discussed above separated by (F606w–F814w) $= -0.15$. For the Centaur and low-q subsets, the probability that the sample consists of a single population is 14% and 30%, respectively.

We note that the DIP test was sufficient to reveal the bifurcation in the observed ground-based colors of the Centaurs

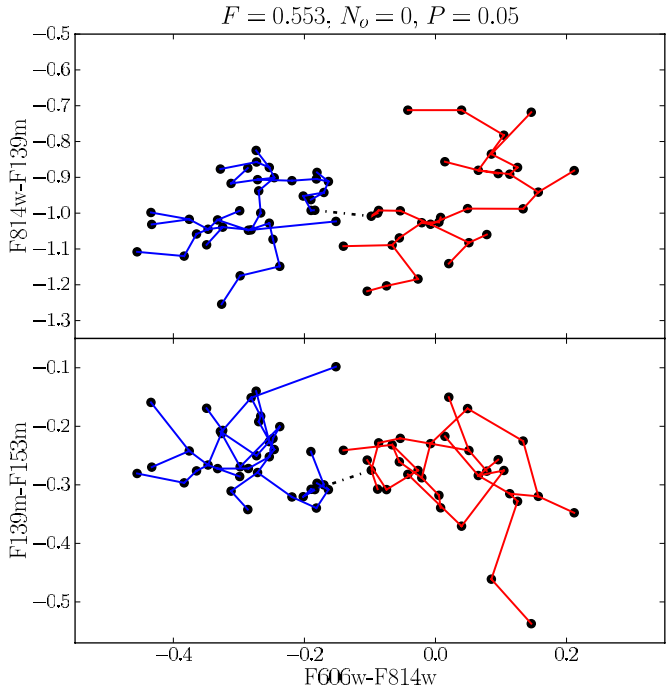

Figure 14. Results of the FOP-test and MSDR clustering to the (F814w–F139m) and (F139m–F154m) vs. (F606w–F814w) colors of non-CCO, non-family member objects with $H > 5.6$ and error in (F814w–F139m) less than 0.1 mag. Error bars are omitted for clarity. The edges of the minimum spanning tree are shown as line segments. The dotted segment shows the pruned edge identified by both techniques, resulting in the two clusters identified by the blue and red segments. The F, N_o, and the probability that the sample consists of only one population from the FOP-test are shown. Both techniques agree with our assertion that most of the small, excited KBOs exhibit bifurcation into two separate classes at a color of (F606w–F814w) ~ -0.15.

(A color version of this figure is available in the online journal.)

from their optical data alone with a sample size similar to what we present here. This is most likely a result of the use of the $(B-R)$ color where the bifurcation is most prominent having a width of $\sim$0.3 mag between the two groups (see Figure 5). Thus, further confirmation of our result could be provided with additional observations at $\sim$0.5 μm.

The results of all five separate statistics, the DIP test, the FOP-test, and hierarchical, normal mixture model, and MSDR clustering, are all in agreement—the colors of the small, excited KBOs are bifurcated. Indeed, the four separate clustering methods produce nearly identical results, with only the normal mixture model results differing from the other three methods, producing the same two main clusters and a third small cluster of outliers. The results of these blind statistical tests support our assertion above, that these objects fall into two compositional classes, the colors of which are described by two branches of a simple two-component compositional mixing model. This result solves a long-standing issue with the Centaurs, the colors of which appeared different from the other excited populations that are ultimately responsible for replenishing the dynamically short-lived Centaurs. We find the simple idea that all small, excited KBOs fall into one of two compositional classes a pleasing result.

4. DISCUSSION

The primary result from this survey is the demonstration that other than the CCOs, the Haumea family members, and those objects with $H < 5.6$, the small, excited KBOs fall into two separate composition classes, the colors of which are well described by two separate intimate mixtures, both of which share the same neutral component. These results have profound consequences for our understanding of the formation of the Kuiper Belt and are indicative of two unique primordial locations from which each class formed.

4.1. The Colors of the Kuiper Belt

Our observations suggest that the small excited Kuiper Belt populations that include the Centaurs, scattered disk, resonant, and HCOs fall into two separate compositional classes, the colors of which are determined by the relative composition an object has within its class. In addition, our observations suggest that little surface evolution occurs as an object evolves from an excited orbit into the Centaur population. This suggests that both classes of objects must have existed within the primordial planetesimal disk before the occurrence of the scattering event that emplaced these objects in the Kuiper Belt.

One possible explanation for the primordial existence of two classes of objects is presented in Brown et al. (2011b), who have shown that the methanol sublimation line exists at $\sim$20 AU, roughly within the primordial disk from which the excited KBOs are believed to have originated. They demonstrated that methanol ice could survive on planetesimal surfaces outside of $\sim$20 AU, while inside this distance, methanol sublimation is rapid enough to deplete all surface methanol before the scattering event occurred. Methanol is an important organic ice, as solar irradiance can drive methanol chemistry to produce longer chain hydrocarbons. Surface processing would produce a red irradiated mantel of complex hydrocarbons on roughly Myr timescales, resulting in a red appearance. Objects that spent most of their time inside of 20 AU were unable to retain methanol, resulting in a neutral surface free of a red irradiation mantel. Despite the attractiveness of this model, alternate explanations for the two unique surfaces are possible.

We have found that the blue and red mixing models do not describe the colors of objects with $H_{606} \lesssim 5.6$. This roughly corresponds to a diameter of $D \sim$ 300–400 km. Our findings are in agreement with albedo observations that suggest that objects larger than $D \sim$ 400 km have higher albedos than those smaller objects (Stansberry et al. 2008). These results point to a fundamental difference in the surface properties of objects with diameters $D \gtrsim 400$ km. These intermediate-sized objects also exhibit different surfaces than the volatile bearing objects with $D \gtrsim 1000$ km. It seems that the surfaces of the intermediate-sized objects are dominated by other processes that have little effect at smaller sizes. These could include the onset of differentiation or cryovolcanic processes, both of which would have the effect of covering or removing non-icy materials from the surface.

The CCOs exhibit a unique surface with different albedos than either class of excited KBO. As these objects most likely formed nearly in situ, it appears that the primordial disk from which all KBOs formed generally consisted of three separate classes of small object. The colors of the CCOs are formally compatible with the red branch of the mixing model. A simple explanation for this is that both populations formed adjacent to one another in the primordial disk. Due to their larger formation distance, however, the classical objects accreted material with a slightly different composition than did the red excited objects. Brown et al. (2011b) suggest that the CCOs may possess a significantly higher fraction of NH_3 compared to the excited populations. While it is not clear what effects variations in NH_3 content

might have on an object's appearance, it seems reasonable to think that the existence of primordial ices not likely retained by the red excited objects could result in a different surface.

4.2. The Nature of the Mixture Components

Little can be said about the red components of each mixing branch from our observations alone. Other spectroscopic studies, however, provide some additional guidance. In modeling observed spectra, the red optical color of KBOs is usually attributed to irradiated organic material and tholins produced in the laboratory and seen on other icy bodies (see, for example, Cruikshank et al. 1991; Brunetto et al. 2006; Filacchione et al. 2007). In addition, absorption at $\sim$1.5 μm is often attributed to water ice. The range of colors compatible with our data is similar to those produced in spectral modeling of these ices (Cruikshank et al. 1998; Merlin et al. 2010; Barucci et al. 2011). Thus, combinations of irradiated organics and water ice are likely red candidates.

The existence of a common neutral component for both branches implies that this material was prevalent throughout the protoplanetary disk both interior to and exterior to the methanol sublimation line. As discussed above, the best-fit neutral color is consistent with silicate materials inferred to be present on other KBOs (Merlin et al. 2010), including various aqueous altered silicates. Such a result would imply the existence of liquid water in objects in the outer solar system at some point in the past. Our findings are consistent with other works that suggest the existence of aqueous alteration in KBOs (Alvarez-Candal et al. 2008) and comets (Stodolna et al. 2010). This result is surprising as it is expected that only the largest KBOs would have ever possessed large quantities of liquid water at any stage during their histories (McKinnon et al. 2008; Coradini et al. 2008).

One issue still remains with the candidate neutral component, that of albedos. The candidate silicates all have albedos much too high to be compatible with the observed albedos of the small low-q objects. This is consistent with other works that find that to match the low albedos requires the existence of some neutral colored darkening agent (Cruikshank et al. 1998; Barucci et al. 2011). Our results suggest that the relative composition of the darkening agent must not vary significantly compared to the silicate material responsible for the color of the neutral component. Otherwise, two components (neutral and red) would be insufficient to describe the observed colors of either branch.

Our findings suggest that small excited KBOs generally divide into two types. Each type is defined primarily by surface color and can be linked to its formation location within the primordial disk and the mechanism responsible for emplacing that object into the Kuiper Belt. Previous efforts have been made to classify KBOs based on their surface colors. Fulchignoni et al. (2008) present a recent example in which they used G-mode analysis of available ground-based optical and NIR photometry to identify classes of objects. The result was the identification of four separate classes, each with its own unique color. Fulchignoni et al. (2008) attribute the colors of each of their classes to relative amounts of surface evolution experienced by each class's members. The KBO taxons presented in that and other past efforts are fundamentally different from the types we present here, as the objects in both types represent a range of colors rather than one average value. Our interpretations are also different. The mixing models we consider have testable predictions in regard to the spectral shape of objects amongst each class; as one moves redward along a mixing line, the spectra of objects at that color and belonging to that type will vary primarily in a way consistent with an intimate mixture of two component's spectra. Future detailed spectral observations will be able to test this prediction.

The majority of small excited KBOs are consistent with being drawn from two compositional types. The simple compositional model we present, however, has not accounted for a few important effects. The Haumea family demonstrates that collisions can play an important role in modifying the colors of icy bodies. In addition, due to the chaotic nature of the scattering that disrupted the primordial disk, it is possible that a small fraction of KBOs originated from different regions than the primary source populations. While these processes will modify the surfaces in ways not accounted for by our simple picture, their overall effect is not sufficient to hide the existence of the two unique surface types.

5. CONCLUSIONS

We have presented the first results of the H/WTSOSS. The optical and NIR photometry of this project has revealed that the small KBOs with perihelia $q < 35$ AU all exhibit a bifurcated optical color distribution thought previously to be unique only to the Centaurs. Both the red and blue small KBOs exhibit highly correlated optical and NIR colors and clearly define two types of KBO surface. The colors of each surface type are well described by simple two-component mixture models, both of which share a common neutral component but have different red components. The red components are consistent with irradiated organics and tholins seen on other icy bodies. The neutral component is a material that must have pervaded the outer protoplanetary disk, the colors of which are consistent with a range of olivines and aqueously altered silicates.

We have found that the colors of the small $H_{606} > 5.6$ objects of all excited dynamical classes are consistent with the colors of our simple mixing model. This suggests that all small excited KBO populations exhibit the same color distribution and that the bifurcation observed in the colors of the Centaurs must have existed in the primordial disk before whatever scattering event occurred that populated all excited classes of the Kuiper Belt.

The CCOs exhibit an additional unique surface. Despite their consistency in color with red excited objects, their higher albedos and smaller color range suggest that the CCOs and the red excited objects possess different surfaces.

We thank Eric Feigelson for his suggestion to use clustering methods in this project. Support for program HST-GO-11644.01-A was provided by NASA through a grant from the Space Telescope Science Institute, which is operated by the Association of Universities for Research in Astronomy, Inc., under NASA contract NAS 5-26555.

APPENDIX

MINIMUM SPANNING TREE CLUSTERING AND THE FOP-test

Various methods exists to identify clusters within multivariate data. Here, we consider the use of MST-based clustering methods. An MST is an acyclic connected graph of a set of data points that minimizes some weight between pairs of data points. Most common MSTs are Euclidean. That is, a Euclidean MST is the graph that minimizes the total Euclidean distance of the graph's edges. In its most general sense, MST-based clustering algorithms remove or prune *inconsistent* edges from the graph,

resulting in subgraphs, or clusters of the data where the removal of k edges results in $k+1$ clusters. The concept of this approach is simple: if a data set is truly clustered, then only one edge will exist in the MST connecting one cluster to the next.

The key to MST-based clustering lies in the definition of *inconsistent*. While many criteria have been proposed (see Jain et al. 1999, for a review), perhaps the most intuitive is the edge-length-based criterion proposed by Zahn (1971), which simply rejects the largest edges in a tree. While conceptually simple, this method can suffer from chaining between separate clusters preventing those clusters from being identified, or the artificial identification of a cluster caused by some unusually distant data point. Other alternative methods that prune based on deviations about cluster means are also conceptually simple but avoid much of the problems faced by largest edge methods. We adopt the method proposed by Grygorash et al. (2006), which prunes those edges that result in the largest decreases in the weighted standard deviations of cluster members about their cluster means. Grygorash et al. (2006) call this the maximum standard deviation reduction clustering algorithm, or MSDR, and have shown this method to be successful in correctly extracting otherwise complex structures in artificial data.

Two approaches exist to determine the number of clusters in a data set. The first is simply to set the number of clusters a priori. Clearly, this requires prior information about the underlying structure of the data and presents an undesirable situation if that information is unavailable. Alternatively, some stopping criterion can be defined. The stopping criterion chosen by Grygorash et al. (2006) adds additional clusters until the first local minimum in the curve of weighted standard deviation versus k is found, thus providing the *most desirable* number of clusters.

One question still remains with the use of cluster methods that utilize a stopping criterion—are the clusters real or artificial? Most multivariate clustering methods do not assign a significance to the existence of identified clusters. Here, we present a novel approach to the problem with the creation of a new statistic that can be compared to an artificial distribution to generate a significance level for that statistic.

Some of the most easily identified clusters are those that are well separated in the data set—clustering by longest edge, or by average cluster separation, has been proposed as a clustering metrics (Zahn 1971; Hartigan 1981). Distance alone, however, is insufficient. A cluster must additionally be well sampled before its identification may be believed. This led to the RUNT test of multimodality by Hartigan & Mohanty (1992), in which the smallest cluster population size is used as the test statistic, albeit in hierarchical clustering rather than in the MST-based clustering we consider here. It follows that these two metrics, separation and size, could be combined. We propose that a good statistic for quantifying the significance of division of a data set into clusters might be the size of the purported clusters weighted by the distance between them, the latter of which can be found from the pruned edge in the MST. Thus, we define a new statistic as follows. For a set of N points S in $\mathbb{E}^n$ connected by a Euclidean MST T, we divide T into two clusters or subtrees t_1 and t_2 by pruning some edge of T with length l. We define the F statistic of the pruned edge as

$$F = 2\left(\frac{\min\left(|t_1|, |t_2|\right)}{N}\right)\left(\frac{l}{l_{\max}}\right), \tag{A1}$$

where $|t_i|$ is the size of the cluster t_i, and $l_{\max}$ is the Euclidean magnitude of the longest edge in T. F can take on any value in the range (0, 1]. The closer the value is to 1, the more the sample S appears bifurcated. Clearly, such a statistic gives higher weights or biases to divisions that create the largest cluster sizes, a property of many different clustering techniques (Everitt et al. 2011). While not appropriate in all cases, we feel that this metric better reflects reliable divisions by avoiding the creation of many small and unrealistic sub-clusters.

As it is written in Equation (A1), the F statistic can be applied to any MST-based clustering method, regardless of the measure of *inconsistency* or the stopping criterion. Alternatively, F can be combined with additional information to be used as a test for the existence of a bifurcation in a data set. The trick comes from the expectation that an easily identified cluster is one that is well isolated from other clusters, not just at a single point, but across its entire extent. It follows that a surface can be found that optimally divides the regions occupied by two separate clusters. In many cases, the simplest surface is a flat one, that is, a line in $\mathbb{E}^2$, a plane in $\mathbb{E}^3$, etc. Clearly, the flat surface that optimally divides two clusters must intersect with the MST edge that divides them. In addition, this flat surface, which may not be unique, will have the fewest members of each cluster on the wrong side of that plane.

We define the *optimal plane* of two sub-clusters t_1 and t_2 found by pruning edge e from an MST of the data set S as any flat surface that intersects that edge and has the lowest $N_o = n_{o,1} + n_{o,2}$, where $n_{o,i}$ is the number of members of cluster t_i on the wrong side of the optimal plane. We note that the problem can be further simplified by requiring that the optimal surface contains the midpoint of edge e, a simplification we adopt.

The *optimal plane* can be used in conjunction with F to find the most *inconsistent* edge that proves most optimal in dividing a data set. That is, the edge that, upon pruning, creates the two most well-separated clusters is the one that has the *optimal plane* with smallest N_o and largest F. The procedure is then to probe each edge in the MST to find those with the smallest N_o and choose the edge that maximizes F. One distinct disadvantage of the use of the *optimal plane* is the difficulty in identifying the full extent of a curved cluster if another cluster is contained within its curvature. Clearly, the use of the *optimal plane* is not always appropriate. But its simple interpretation makes its use desirable in many situations.

The significance of the resultant division can be determined by two separate methods. The first and most preferable method is to bootstrap the data set by resampling each dimension of the data, independently producing an artificial sample of the same size as the original data. The *optimal plane* and resultant value of F and N_o are then determined from this artificial data set, and the process is repeated to produce the distribution of F and N_o sampled from the observed distribution of the data. The probability of finding an edge with an F-value equal to or larger than that found from the data set *and* an N_o-value equal to or smaller than that found from the data set is determined by giving the probability of the null hypothesis, that is, the probability that the data set is consistent with being drawn from a single population distributed like the observed data.

Alternatively, the observed value of F and corresponding N_o can be compared against the uniform distribution. Formally, this approach tests a different null hypothesis than the bootstrapping method, that the observed F and corresponding N_o are consistent with the distribution drawn from the uniform distribution. This approach, however, is more advantageous than bootstrapping for small data sets, where bootstrapping can produce a biased

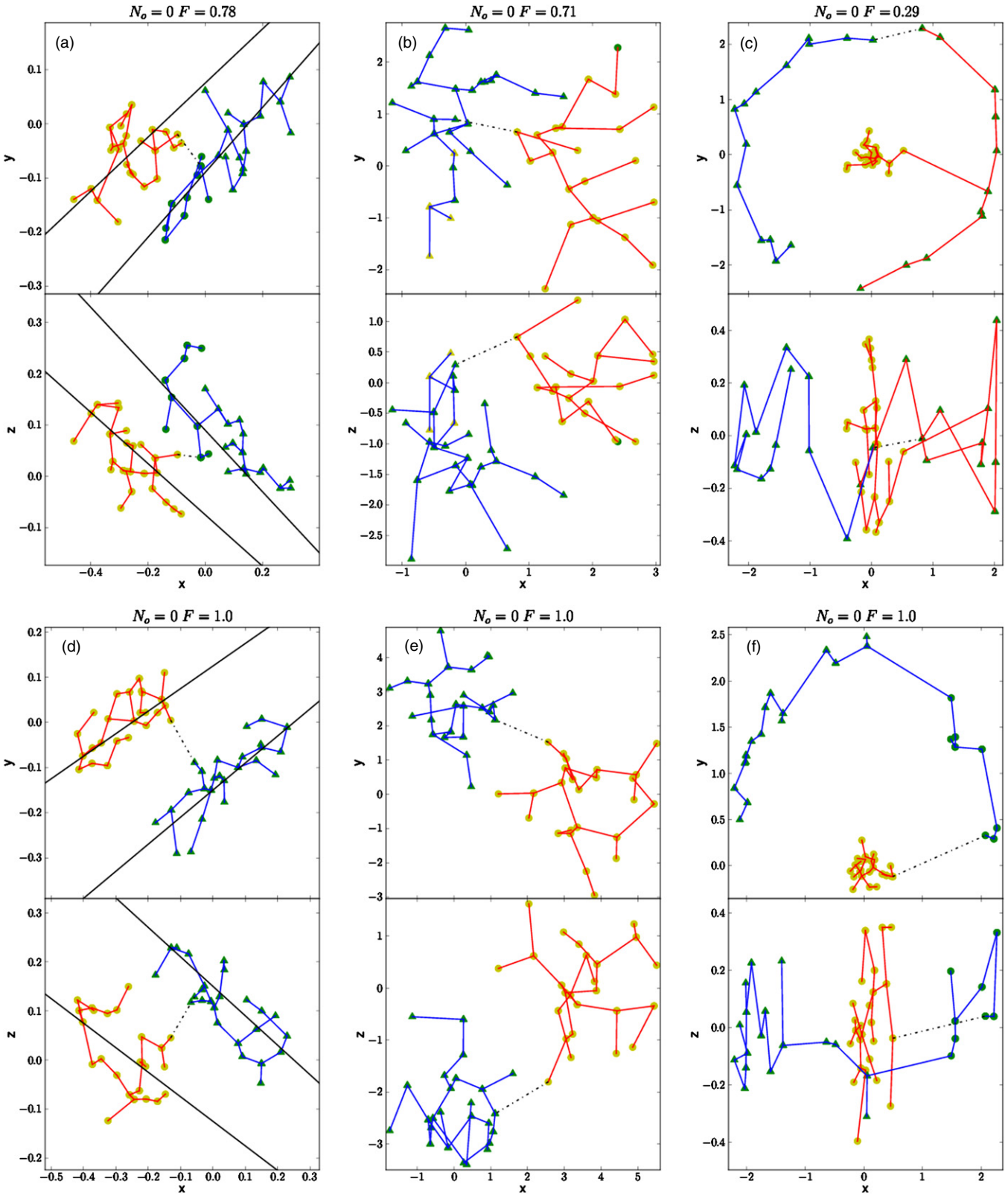

Figure 15. Simulated tests of MSDR clustering and the FOP-test. Triangles and circles represent objects randomly drawn from clusters 1 and 2, respectively. The edges of the minimum spanning tree are shown as line segments. Green and yellow points are members of the first and second samples identified by MSDR. The segment pruned by the FOP-test —that for which the *optimal plane* with maximal F is found—is shown as the dashed line. The red and blue segments show the two sub-clusters as a result of the FOP-test division, and the resultant N_o and F are displayed. (a and d) Samples drawn from two close and distant lines, respectively. The lines from which the points were sampled are shown. (b and d) Samples drawn from three-dimensional normal distributions with distance between the normal means of 2 and 5, respectively. (c) One cluster drawn from a three-dimensional Gaussian with standard deviation 1/3 and the other drawn from a circle with radius 1. (e) Same as in (c) but for a half-circle.

(A color version of this figure is available in the online journal.)

result when the underlying distribution is not well sampled. With either calibration approach, the combined usage of F and the *optimal plane* provides a test of the existence of a bifurcation in the observed data—we call this the FOP-test. We reiterate, however, that for a sufficient sample size—initial tests suggest a sample of 10 or more data points—the bootstrapping approach is nominal.

To show the performance of the MSDR clustering technique and the FOP-test, we present three test cases. For simplicity, we present all test cases in $\mathbb{E}^3$. The first case is a simulated data set made up of two equally sampled normal distributions with different means. The second case is reminiscent of the observations we present in this manuscript. Two different populations are drawn from two lines of different slopes. The last is a special case in which the FOP-test should have difficulty. One cluster is drawn from a normal distribution, while the second is drawn from an annulus centered on and surrounding the normal distribution. In all cases, the sample size is 50, equally split between the two clusters. Two examples at different separations are tested in all cases.

The results of the MSDR clustering technique and the FOP-test are shown in Figure 15. The probability of the null hypothesis associated with the presented tests was determined from the bootstrapping approach and is $<2\%$ for that shown in panels (a)–(e) and 40% for panel (f).

These tests reveal that, in general, the FOP-test performs as well as, or even better than, the MSDR clustering. That is, where the two clusters are well separated, both techniques produce identical results. When the clusters are closer together, however, the FOP-test more frequently identifies the correct edge from which to separate the two clusters, resulting in fewer misclassifications of cluster membership. The second case, that of two lines, is particularly instructive. In the situation where the two samples were generated close together (Figure 15(a)), the FOP-test typically outperformed MSDR in the sense that the FOP-test correctly determined cluster membership for most or all data points much more often than did MSDR, even in cases with low values of F.

As expected, however, the FOP-test performs poorly in the third case, in which one cluster wraps about the other. A typical result was a division of the arc into two sub-clusters with very low F, despite the fact that the correct cluster distribution is clear and easily identified by the MSDR clustering. In the case of a half-arc, the FOP-test could correctly identify the two clusters with very high F, though with low frequency. This result demonstrates the primary weakness of the FOP-test in that the test implicitly assumes that the clusters can be well separated by some plane.

The performance of the FOP-test was also significantly diminished when the two generated clusters were not of the same sample size. The tests shown in Figures 15(a) and (d) were performed with 35 and 15 data points in each generated cluster. For case (a) where the lines are furthest separated, the FOP-test performed well, correctly identifying the bifurcation, albeit with higher probability of the null hypothesis. For case (d) with a smaller separation between the lines, the FOP-test failed the majority of the time. This result demonstrates the second weakness of the FOP-test, which weights the results to clusters of nearly equal population. In situations where both weaknesses are avoided, however, the FOP-test performs quite well, even outperforming the successful MSDR clustering technique.

In addition, it should be noted that the FOP-test was not driven by some mathematical properties of MSTs. Rather, the F statistic is an ad hoc combination of two previously suggested clustering metrics, the properties of which remain mathematically unproven. The use of the FOP-test bears this additional caveat. Despite this, however, our simulations demonstrate the ability of the FOP-test to identify the correct clusters at least as well as other techniques.

REFERENCES

Alvarez-Candal, A., Fornasier, S., Barucci, M. A., de Bergh, C., & Merlin, F. 2008, A&A, 487, 741
Barkume, K. M., Brown, M. E., & Schaller, E. L. 2008, AJ, 135, 55
Barucci, M. A., Alvarez-Candal, A., Merlin, F., et al. 2011, Icarus, 214, 297
Barucci, M. A., Boehnhardt, H., Cruikshank, D. P., & Morbidelli, A. 2008, in The Solar System beyond Neptune, ed. M. A. Barucci, H. Boehnhardt, D. P. Cruikshank, & A. Morbidelli (Tucson: Univ. Arizona Press), 143
Benecchi, S. D., Noll, K. S., Grundy, W. M., et al. 2009, Icarus, 200, 292
Benecchi, S. D., Noll, K. S., Stephens, D. C., Grundy, W. M., & Rawlins, J. 2011, Icarus, 213, 693
Bernstein, G. 2008, Minor Planet Center Orbit Data Base, http://www.cfa.harvard.edu/iau/MPCORB.html
Brown, M. E. 2001, AJ, 121, 2804
Brown, M. E., Barkume, K. M., Ragozzine, D., & Schaller, E. L. 2007, Nature, 446, 294
Brown, M. E., Burgasser, A. J., & Fraser, W. C. 2011a, ApJ, 738, L26
Brown, M. E., Schaller, E. L., & Fraser, W. C. 2011b, ApJ, 739, L60
Brucker, M. J., Grundy, W. M., Stansberry, J. A., et al. 2009, Icarus, 201, 284
Brunetto, R., Barucci, M. A., Dotto, E., & Strazzulla, G. 2006, ApJ, 644, 646
Clark, R. N., Brown, R. H., Jaumann, R., et al. 2005, Nature, 435, 66
Clark, R. N., Swayze, G. A., Wise, R., et al. 2007, USGS Digital Spectral Library splib06a: U.S. Geological Survey, Digital Data Series 231, http://speclab.cr.usgs.gov/spectral.lib06
Coradini, A., Capria, M. T., de Sanctis, M. C., & McKinnon, W. B. 2008, in The Solar System beyond Neptune, ed. M. A. Barucci, H. Boehnhardt, D. P. Cruikshank, & A. Morbidelli (Tucson: Univ. Arizona Press), 243
Cruikshank, D. P., Allamandola, L. J., Hartmann, W. K., et al. 1991, Icarus, 94, 345
Cruikshank, D. P., Pilcher, C. B., & Morrison, D. 1976, Science, 194, 835
Cruikshank, D. P., Roush, T. L., Bartholomew, M. J., et al. 1998, Icarus, 135, 389
Doressoundiram, A., Peixinho, N., de Bergh, C., et al. 2002, AJ, 124, 2279
Duffard, R., Ortiz, J. L., Thirouin, A., Santos-Sanz, P., & Morales, N. 2009, A&A, 505, 1283
Elliot, J. L., Kern, S. D., Clancy, K. B., et al. 2005, AJ, 129, 1117
Everitt, B., Landau, S., Leese, M., & Stahl, D. 2011, Cluster Analysis (Wiley Series in Probability and Statistics; Chichester, UK: Wiley)
Filacchione, G., Capaccioni, F., McCord, T. B., et al. 2007, Icarus, 186, 259
Fornasier, S., Barucci, M. A., de Bergh, C., et al. 2009, A&A, 508, 457
Fraser, W. C., Kavelaars, J. J., Holman, M. J., et al. 2008, Icarus, 195, 827
Fulchignoni, M., Belskaya, I., Barucci, M. A., de Sanctis, M. C., & Doressoundiram, A. 2008, in The Solar System beyond Neptune, ed. M. A. Barucci, H. Boehnhardt, D. P. Cruikshank, & A. Morbidelli (Tucson: Univ. Arizona Press), 181
Georgi, B., Costa, I. G., & Schliep, A. 2010, BMC Bioinform., 11, 9
Gladman, B., Marsden, B. G., & Vanlaerhoven, C. 2008, in The Solar System beyond Neptune, ed. M. A. Barucci, H. Boehnhardt, D. P. Cruikshank, & A. Morbidelli (Tucson: Univ. Arizona Press), 43
Grygorash, O., Zhou, Y., & Jorgensen, Z. 2006, in 18th IEEE Int. Conf. on Tools with Artificial Intelligence ICTAI06, ed. S. Ceballos (Los Alamitos, CA: The Institute of Electrical and Electronics Engineers, Inc.), 73
Guilbert, A., Alvarez-Candal, A., Merlin, F., et al. 2009, Icarus, 201, 272
Hainaut, O. R., & Delsanti, A. C. 2002, A&A, 389, 641
Hapke, B. 2002, Icarus, 157, 523
Hartigan, J., & Mohanty, S. 1992, J. Classif., 9, 63
Hartigan, J. A. 1981, J. Am. Stat. Assoc., 76, 388
Hartigan, J. A., & Hartigan, P. M. 1985, Ann. Stat., 13, 70
Jain, A. K., Murty, M. N., & Flynn, P. J. 1999, ACM Comput. Surv., 31, 264
Jewitt, D. C., & Luu, J. X. 2001, AJ, 122, 2099
Krist, J. 1993, in ASP Conf. Ser. 52, Astronomical Data Analysis Software and Systems II, ed. R. J. Hanisch, R. J. V. Brissenden, & J. Barnes (San Francisco, CA: ASP), 536
Levison, H. F., Morbidelli, A., Vanlaerhoven, C., Gomes, R., & Tsiganis, K. 2008, Icarus, 196, 258
Luu, J., & Jewitt, D. 1996, AJ, 112, 2310
Lykawka, P. S., & Mukai, T. 2007, Icarus, 189, 213

Malhotra, R. 1993, Nature, 365, 819
McKinnon, W. B., Prialnik, D., Stern, S. A., & Coradini, A. 2008, in The Solar System beyond Neptune, ed. M. A. Barucci, H. Boehnhardt, D. P. Cruikshank, & A. Morbidelli (Tucson: Univ. Arizona Press), 213
Merlin, F., Barucci, M. A., de Bergh, C., et al. 2010, Icarus, 208, 945
Morbidelli, A., Levison, H. F., & Gomes, R. 2008, in The Solar System beyond Neptune, ed. M. A. Barucci, H. Boehnhardt, D. P. Cruikshank, & A. Morbidelli (Tucson: Univ. Arizona Press), 275
Nesvorný, D., Vokrouhlický, D., & Morbidelli, A. 2007, AJ, 133, 1962
Newberry, M. V. 1991, PASP, 103, 122
Peixinho, N., Boehnhardt, H., Belskaya, I., et al. 2004, Icarus, 170, 153
Peixinho, N., Lacerda, P., & Jewitt, D. 2008, AJ, 136, 1837
Press, W. H. 2002, Numerical Recipes in C++: The Art of Scientific Computing, Vol. xxviii (Cambridge: Cambridge Univ. Press), 1002
Rajan, A., Quijano, J. K., Bushouse, H., & Deustua, S. 2010, WFC3 Data Handbook V2 (Baltimore, MD: StSci)
Schaller, E. L., & Brown, M. E. 2007a, ApJ, 670, L49
Schaller, E. L., & Brown, M. E. 2007b, ApJ, 659, L61
Schaller, E. L., & Brown, M. E. 2008, ApJ, 684, L107
Snodgrass, C., Carry, B., Dumas, C., & Hainaut, O. 2010, A&A, 511, A72
Stansberry, J., Grundy, W., Brown, M., et al. 2008, in The Solar System beyond Neptune, ed. M. A. Barucci, H. Boehnhardt, D. P. Cruikshank, & A. Morbidelli (Tucson: Univ. Arizona Press), 161
Stodolna, J., Jacob, D., & Leroux, H. 2010, in Lunar and Planetary Institute Science Conference Abstracts, Technical Report, Vol. 41, 1657
Tegler, S. C., Bauer, J. M., Romanishin, W., & Peixinho, N. 2008, in The Solar System beyond Neptune, ed. M. A. Barucci, H. Boehnhardt, D. P. Cruikshank, & A. Morbidelli (Tucson: Univ. Arizona Press), 105
Tegler, S. C., & Romanishin, W. 2003, Icarus, 161, 181
Trujillo, C. A., & Brown, M. E. 2001, APJ, 554, L95
Zahn, C. T. 1971, IEEE Trans. Comput., C-20, 68